Revisiting daily MODIS evapotranspiration algorithm using flux tower measurements in China

Lei Huang[12], Tammo S. Steenhuis[2*], Yong Luo[1*], Qiuhong Tang[3,5], Ronglin Tang[4,5], Junqing Zheng[1], Wen Shi[1] and Chen Qiao[1]

[1]Ministry of Education Key Laboratory for Earth System Modeling, Department of Earth System Science, Tsinghua University, Beijing, China.

[2]Department of Biological and Environmental Engineering, Cornell University, Ithaca, NY, USA

[3]Key Laboratory of Water Cycle and Related Land Surface Processes, Institute of Geographic Sciences and Natural Resources Research, Chinese Academy of Sciences, Beijing, China.

[4]State Key Laboratory of Resources and Environment Information System, Institute of Geographic Sciences and Natural Resources Research, Chinese Academy of Sciences, Beijing 100101, China.

[5]University of Chinese Academy of Sciences, Beijing 100049, China.

Corresponding author: Tammo S. Steenhuis (tammo@cornell.edu)
Yong Luo (Yongluo@mail.tsinghua.edu.cn)

Key Points:

Improved satellite-based daily evapotranspiration calculations for China

Decoupling parameter based daily evapotranspiration fraction algorithm

Abstract

Evapotranspiration (ET) is the major component of the hydrology cycle. Satellites provide a convenient way for gathering information to estimate regional ET. The most widely applied method for converting the instantaneous satellite measurement to daily scale assumes that evaporative fraction (EF), defined as the ratio of ET to the available energy, is constant during the daytime. However, this method was proved to underestimate the daily ET. This study implemented a theoretically improved EF algorithm to calculate daily ET with the decoupling factor method based on the Penman-Monteith and McNaughton-Jarvis equations. Seven improved algorithms were developed by assuming that various parameters remain constant during the day. The satellite-based ET estimates were compared with seven local flux tower measurements in China. The results showed that: (1) The original ET method calculated the daily evaporation more accurately than the other algorithms. However, the good fit was based on two compensating inaccuracies. Compared to the flux tower measurement, the original ET method underestimated the daily EF by 26% and overestimated the daily net radiation by 30%. (2) Six of the seven proposed algorithms underpredicted the daily ET by 30-60%, mainly due to the inaccurate daily net radiation. (3) The algorithm that assumed that the instantaneous decoupling parameter Ω was equal to its daily value method calculated EF and ET with the relative errors of 8% and 10% when the inaccurate estimated daily net radiation was replaced by the observed flux tower data.

Plain Language Summary

The water that evaporates from the land surface sustains the hydrological cycle that replenishes the world's freshwater resources. Scientists and water managers are therefore interested in quantifying the water that evaporates each day. It is especially true for China that has one of the lowest water reserves in the world. Satellites that provide coverage of all the land surface would be ideal for recording evaporation if we could scale up the instantaneous satellite measurements to a daily scale. The

current scale-up methods available have not been widely tested. In this manuscript, we test the available methods and show how they can be improved for China.

1 Introduction

In the seventeenth century, the first water balance was made for the Seine by Perrault (1674). Since that time, it became apparent that evapotranspiration (ET) sustains the hydrologic cycle and replenishes the world's freshwater resources (Katul and Novick, 2009). Today, evaporation is a critical component of the short-term numerical weather predication, long-term climate simulations, and diagnoses of climate change (Brutsaert et al., 2019; Jung et al., 2019; Wang & Dickinson, 2012).

Products of actual evaporation are usually from ground measurements, climate (or hydrology) model output, or satellite-based estimates. Ground measurements like flux towers and lysimeters can make ground or point scale evaporation measurements. Pan evaporation can be used for point scale but needs to be adjusted for the soil moisture content using a model such as the Thornthwaite Mater Procedure (Portela et al., 2019; Steenhuis & van der Molen, 1982). The climate and hydrology models could provide large-scale and long-time ET estimates, but they often have coarse resolutions and assuming the land cover was fixed, leading to large uncertainties. Satellite measurements can calculate regional-scale evaporation at low-cost (Miranda et al., 2017), and unlike the climate models, they have higher resoluation and more realistic land parameters. Moderate Resolution Imaging Spectroradiometer (MODIS) (Ait Hssaine et al., 2020; Faisol et al., 2020; Mu et al., 2007, 2011; Zhang et al., 2019), Advanced Very High-Resolution Radiometer (AVHRR) (Dile et al., 2020; Zhang et al., 2009, 2010) and Landsat (Allen Richard G. et al., 2007; Bastiaanssen, Menenti, et al., 1998; Bastiaanssen, Paul, et al., 2020) have tabulated over the past 20 years, and they provided pioneering satellite-based regional ET estimates models.

Evapotranspiration for large basins or countries by remote sensing methods is calculated by extrapolating instantaneous remotely sensed satellite measurements (usually taken around midday) over daily or more extended periods (Hou et al., 2019; Zou et al., 2018). Several published methods convert the instantaneous ET

measurements to the daily evaporation: constant evaporative fraction method (Brutsaert & Sugita, 1992), reference evaporative fraction method (Tang et al., 2017), constant ET-radiation radio methods, including the ET-top-of-atmosphere irradiance (Cammalleri et al., 2014), ET-extraterrestrial solar irradiance (Ryu et al., 2012) and ET -insolation method (Knipper et al., 2020). These methods vary for the various climates, and land uses, in almost cases, require calibration when applied to a different region (Alfieri et al., 2017; Chen & Liu, 2020; Delogu et al., 2012).

The most widely used method to convert instantaneous satellite measurements to daily values is called the evaporation fraction (*EF*) method. The *EF* is defined as the ratio of *ET* to the available energy flux, *Q* which is the sum of *ET* and sensible heat flux (Brutsaert & Sugita, 1992; Shuttleworth, 1989; Sugita & Brutsaert, 1991). This method assumes that the *EF* remains constant during the day (Nichols & Cuenca, 1993) and thus the daily latent heat flux (e.g., evaporation) is calculated as the product of the daily mean available energy *Q* and *EF* (Chen & Liu, 2020; Hu et al., 2019).

Researchers have, however, shown the *EF* is not constant during the daytime (Gentine et al., 2007; Liu et al., 2020; Panwar et al., 2020; Sobrino et al., 2007). Using the instantaneous constant *EF* during the midday as its daily mean value will underestimate the daily *ET* by 5%-30% (Farah et al., 2004; Van Niel et al., 2011, 2012; Yang et al., 2013). The *EF* depends on several environmental factors including saturation deficit above the well-mixed layer (Lhomme & Elguero, 1999), the solar radiation intensity, friction velocity, water availability, relative humidity, cloudiness, and boundary layer entrainment (Gentine et al., 2011)

To avoid underestimating the daily *ET* with the *EF* method, Tang & Li (2017) introduced a new method to calculate the *ET* based on an extra Penman-Monteith's expanded form Priestley-Taylor equation. They expressed the *EF* as a function of ratios of daily and instantaneous measured values of the slope of the saturated vapor pressure, the psychometric constant, and a decoupling factor representing the relative contribution of the radiative and aerodynamic terms to the overall *ET*. Tang & Li (2017) tested their method in the cropped and irrigated North China Plain using

instantaneous satellite measurements and ground-based daily observations. They found that the daily ET calculated by their method was more robust and accurate than the constant EF method.

Our objective is to improve daily evaporation accuracy from instantaneous satellite measurements by adapting Tang & Li (2017) method for land uses other than irrigated cropland. The improved method is tested by comparing the flux tower measurements in China with evapotranspiration and several intermediate variables calculated with datasets of the Moderate Resolution Imaging Spectroradiometer (MODIS) Land Product and China Meteorological Forcing. The intermediate tested variables are instantaneous and daily air temperature and net radiation, and the daily EF. The MODIS Land Product has a spatial resolution of 0.05 degree and the China Meteorological Forcing data has a resolution of 0.1 degrees.

2. Theory

2.1 Evaporative fraction

Satellites provide only instantaneous data at fixed intervals that can range from several times a day to once in several days. To extend the instantaneous data to daily values, Nishida et al. (2003) assumed that the instantaneously measured evaporation fraction, EF^i during the satellite overpass around noon time was equal to the daily evaporation fraction EF^d. The EF, that was originally introduced by Brutsaert & Sugita, (1992) for calculation of evaporation in Kansas with weather balloons, is defined for both instantaneous and daily measurements as the ratio of latent heat flux (ET) to available energy flux, Q (W m^{-2}):

$$EF = \frac{ET}{Q} \tag{1}$$

where ET is the actual evapotranspiration (W m^{-2}); Q is the sum of the latent heat flux and sensible heat flux, also called the available energy (W m^{-2}). The evapotranspiration, ET, can be calculated as the sum of the transpiration from the vegetation and the evaporation from the bare soil surface when the energy transfer from the vegetation to the soil surface can be neglected (Nishida et al., 2003), i.e.,

$$ET ¿ f_{veg} ET_{veg} + (1 - f_{veg}) ET_{soil} \quad (2)$$

where the subscript "*veg*" means full vegetation cover and subscript "***soil***" indicates the soil exposed to solar radiation (called bare soil); ET_{veg} is the transpiration from the full vegetation cover (W m^{-2}), ET_{soil} is the evaporation from the soil (W m^{-2}), f_{veg} is the portion of the area with the vegetation cover. The equation and the method for calculating f_{veg} is given in Appendix A. The available energy Q (W m^{-2}) is expressed by Nishida et al. (2003) as:

$$Q ¿ f_{veg} Q_{veg} + (1 - f ¿¿ veg) Q_{soil} ¿ \quad (3)$$

where Q_{veg} is the available energy for the vegetation (W m^{-2}) and Q_{soil} is the available energy for bare soil (W m^{-2}). Equations 1-3 are valid over any period, including instantaneous and daily times.

The instantaneous evaporation fraction, EF^i may be found by combining Eqs. 1, 2, and 3 as:

$$EF^i ¿ f_{veg} \frac{Q^i_{veg}}{Q^i} EF^i_{veg} + (1 - f ¿¿ veg) \frac{Q^i_{soil}}{Q^i} EF^i_{soil} ¿ \quad (4)$$

where the superscript *i* stands for the instantaneous value of the parameter, EF^i_{veg} and EF^i_{soil} are the instantaneous evaporation fractions for the vegetation and bare soil, respectively. Combing the complementary relationship as described by Bouchet (1963), Morton (1978), Brutsaert and Stricker (1979), and Nishida et al. (2003):

$$ET + PET = 2 ET_0 \quad (5)$$

PET is the potential ET (W m^{-2}), described by the Penman-Monteith potential ET equations, ET_0 is the ET when ET equals to the potential ET (W m^{-2}), described by the Priestley-Taylor equation, the EF^i_{veg} can be expressed as a function of instantaneously measured parameters as:

$$EF_{veg}^{i} = \frac{\alpha \Delta^{i}}{\Delta^{i} + \gamma\left(1 + r_{c\,veg}^{i} / 2 r_{a\,veg}^{i}\right)} \quad (6)$$

where α is the Priestley-Taylor parameter which was set to 1.26 (De Bruin, 1983); Δ^{i} is the slope of the saturated vapor pressure, which is a function of the temperature (Pa K^{-1}; γ is the psychometric constant (Pa K^{-1}); $r_{c\,veg}^{i}$ is the instantaneous surface resistance of the vegetation canopy (s m^{-1}); $r_{a\,veg}^{i}$ is the instantaneous aerodynamics resistance of the vegetation canopy (s m^{-1}). Expressions for the surface and the aerodynamic resistances and slope of the saturated vapor pressure can be found in Appendices B and D.

Assuming that the evaporation fraction of bare soil is constant during the day, EF_{soil}^{i} was expressed by Nishida et al. (2003) as a function of the instantaneous soil temperature and the available energy based on the energy balance of the bare soil:

$$EF_{soil}^{i} = \frac{T_{soil\,max}^{i} - T_{soil}^{i}}{T_{soil\,max}^{i} - T_{a}^{i}} \frac{Q_{soil0}^{i}}{Q_{soil}^{i}} \quad (7)$$

where $T_{soil\,max}^{i}$ is the instantaneous maximum possible temperature at the surface reached when the land surface is dry (K), T_{soil}^{i} is the instantaneous temperature of the bare soil (K), T_{a}^{i} is the instantaneous air temperature, $Q_{soil\,0}^{i}$ is the instantaneous available energy when T_{soil}^{i} is equal to T_{a}^{i} (W m^{-2}).

2.2 Daily evaporation fraction values based on decoupling parameter

Huang et al. (2017) observed that the Nishida (2003) instantaneous midday evaporative fraction, EF^{i} underestimated the daily EF^{d}. To correct for the underprediction, Tang & Li (2017) introduced a new expression based on the Penman-

Monteith equation and McNaughton-Jarvis equation to calculate the daily EF^d that is more generally known as the decoupling factor method:

$$EF^d = EF^i \frac{\Delta^d}{\Delta^d+\gamma} \frac{\Delta^i+\gamma}{\Delta^i} \frac{\Omega^{¿i}}{\Omega^{¿d}} \frac{\Omega^d}{\Omega^i} \quad (8)$$

where superscript "d" means daily; the EF^i is the midday instantaneous evaporation fraction; Ω is decoupling factor that represents the relative contribution of radiative and the aerodynamic terms to the overall evapotranspiration (McNaughton & Jarvis, 1983), $\Omega_i^{¿}$is the value of the decoupling factor, Ω, for wet surfaces. According to Pereira (2004), Ω and $\Omega^{¿}$ can be expressed as:

$$\Omega = \frac{1}{1+\frac{\gamma}{\Delta+\gamma}\frac{r_c}{r_a}} \quad (9)$$

$$\Omega^{¿} = \frac{1}{1+\frac{\gamma}{\Delta+\gamma}\frac{r^{¿}}{r_a}} \quad (10)$$

$$r^{¿} = \frac{(\Delta+\gamma)\rho C_p VPD}{\Delta\gamma(R_n-G)} \quad (11)$$

where r_c is the surface resistance (s m-1); r_a is the aerodynamic resistance (s m^{-1}); $r^{¿}$ is the critical surface resistance when the actual evapotranspiration equals the potential evaporation, (called equilibrium evapotranspiration, s m^{-1}); ρ is the air density (kg m^{-3}); C_p is the specific heat of the air (J kg^{-1} K^{-1}); VPD is the vapor pressure deficit of the air (Pa). The method to calculate the slope of the saturated vapor pressure Δ is specified in Eq. B1; the calculation of vapor deficit, VPD, from satellite data is described in Appendix B with Eqs B2- B5. The resistance factors are further detailed in Appendix D.

The decoupling method (Eq. 8) performed well for irrigated cropland (Tang et al., 2017; Tang & Li, 2017). In this study, we were interested in finding the evaporation of all landscapes. Thus, we need to adapt Eq. 8 for other land uses such as grassland and forest. To do this, the constant EF_{veg} in Eq. 6 and EF_{soil} in Eq. 7 are reformulated similarly to the decoupling method in Eq 8:

$$EF^d_{veg} = \frac{\alpha \Delta^i}{\Delta^i + \gamma \left(1 + \frac{r^i_{c\,veg}}{2 r^i_{a\,veg}}\right)} \left(\frac{\Delta^d}{\Delta^d + \gamma} \frac{\Delta^i + \gamma}{\Delta^i} \frac{\Omega^{¿\,i}_{veg}}{\Omega^{¿\,d}_{veg}} \frac{\Omega^d_{veg}}{\Omega^i_{veg}} \right) \quad (12)$$

$$EF^d_{soil} = \frac{T^i_{soil\,max} - T^i_{soil}}{T^i_{soil\,max} - T^i_a} \frac{Q^i_{soil\,0}}{Q^i_{soil}} \left(\frac{\Delta^d}{\Delta^d + \gamma} \frac{\Delta^i + \gamma}{\Delta^i} \frac{\Omega^{¿\,i}_{soil}}{\Omega^{¿\,d}_{soil}} \frac{\Omega^d_{soil}}{\Omega^i_{soil}} ¿ \right. \quad (13)$$

Substituting EF^d_{veg} (Eq. 12) and EF^d_{soil} (Eq. 13) into Eq. 4:

$$EF^d ¿ f_{veg} \frac{Q^i_{veg}}{Q^i} EF^d_{veg} + (1 - f ¿¿ veg) \frac{Q^i_{soil}}{Q^i} EF^d_{soil} ¿ \quad (14)$$

According to Eq. 1, the daily evaporation ET^d is:

$$ET^d = EF^d Q^d \quad (15)$$

In practice, the instantaneous parameter value for calculating EF^d and ET^d in Eqs 12-15 are often not very precise when derived from the available satellite measurements. We, therefore, introduced eight approximations to determine the daily averaged evaporation fraction EF^d and evaporation ET^d and then tested how well these approximations could reproduce independently measured EF and ET values with flux tower data (Table 1). The first method in Table 1, named ETd, computed the evaporation with all the daily and instantaneous parameters in Eq. 12 and 13. The subsequent methods in Table 1, named ET0-ET7, used various approximations to find daily parameters. The second approximation, ET0, in Table 1 is Nishida's method (2003, Eq 6). It assumed that the daily values were equal to the instantaneously measured values during satellite overpass. Other methods used various ways to approximate the daily values. They included the slope of saturated vapor pressure vs. air temperature, ET1, the surface resistance, aerodynamic resistance, decoupling parameter resistance ET2-ET4, and decoupling factors, ET5 - ET7 (Table 1).

Table 1. Equations for the complete methods using all instantaneous values. EFd, the Nishida (2003) method EF0, and seven approximations EF1-EF7 for calculating the daily values EF^d from the instantaneous evaporation fraction EF^i, based on Eqs 11-14 The superscript d indicates a daily value and the superscript *i* the instantaneous value.

EF	Assumption	Equation	ET

EFd	*No assumptions*	$\mathrm{EFd} = EF^i \frac{\Delta^d}{\Delta^d+\gamma} \frac{\Delta^i+\gamma}{\Delta^i} \frac{\Omega^{¿i}}{\Omega^{¿d}} \frac{\Omega^d}{\Omega^i}$	*ETd*
EF0	$EF^i = EF^d$	$EF\,0 = EF^i$	*ET0*
EF1	$\Delta^i = \Delta^d$	$EF\,1 = EF^i \frac{\Omega^{¿i}}{\Omega^{¿d}} \frac{\Omega^d}{\Omega^i}$	*ET1*
EF2	$r_c^i = r_c^d$	$\mathrm{EF2} = EF^i \frac{\Delta^d}{\Delta^d+\gamma} \frac{\Delta^i+\gamma}{\Delta^i} \frac{\Omega^{¿i}}{\Omega^{¿d}} \frac{\Omega^d}{\Omega^i}$	*ET2*
EF3	$r_c^i = r_c^d$	$\mathrm{EF3} = EF^i \frac{\Delta^d}{\Delta^d+\gamma} \frac{\Delta^i+\gamma}{\Delta^i} \frac{\Omega^{¿i}}{\Omega^{¿d}} \frac{\Omega^d}{\Omega^i}$	*ET3*
EF4	$r^{¿i} = r^{¿d}$	$\mathrm{EF4} = EF^i \frac{\Delta^d}{\Delta^d+\gamma} \frac{\Delta^i+\gamma}{\Delta^i} \frac{\Omega^{¿i}}{\Omega^{¿d}} \frac{\Omega^d}{\Omega^i}$	*ET4*
EF5	$\Omega^i = \Omega^d$	$EF\,5 = EF^i \frac{\Delta^d}{\Delta^d+\gamma} \frac{\Delta^i+\gamma}{\Delta^i} \frac{\Omega^{¿i}}{\Omega^{¿d}}$	*ET5*
EF6	$\Omega^{¿i} = \Omega^{¿d}$	$EF\,6 = EF^i \frac{\Delta^d}{\Delta^d+\gamma} \frac{\Delta^i+\gamma}{\Delta^i} \frac{\Omega^d}{\Omega^i}$	*ET6*
EF7	$\frac{\Omega^{¿i}}{\Omega^{¿d}} \frac{\Omega^d}{\Omega^i} = 1$	$EF\,7 = EF^i \frac{\Delta^d}{\Delta^d+\gamma} \frac{\Delta^i+\gamma}{\Delta^i}$	*ET7*

3 Material, methods and data

This section presents the data and the methods used in calculating the satellite-based daily evaporation fraction, EF^d and the daily evaporation ET^d,using Eqs 11-14 with and without the simplifying approximations listed in Table 1. A description of the data available for seven flux towers in China closes this section (Table 2). Note that the MODIS satellite data are available for 250 m, 500 m, and 0.05 degree (approximately 5 km) grids. While the smallest grid size would likely be more representative of the grid tower measurements used for validation, we chose to use the larger size because we intended to develop a method for large areas such as China. Even with the computer capabilities, using the two smallest grids as input would result in excessive amounts of data and computer time. For that reason, we chose the 0.05-degree grid data as input.

3.1 Data used for calculating satellite-based daily EF and ET

The schematic to calculate the evaporation fraction, EF (Eq. 14), and the evaporation ET (Eq. 15) is shown in Figure 1. The input consists of the MODIS Land Product and China Meteorological Forcing datasets (Table 2).

The MODIS data for China were downloaded for 2001 to 2018 from the website https://modis.gsfc.nasa.gov/. The input data consisted of the following instantaneously measured data each day around noon (Figure 1, Table 2a): the surface reflectance (MOD09CMG), surface temperature/emissivity (MOD11C1), albedo (MCD43C3), 16-day NDVI (MOD13C1), and yearly land cover classes compiled from MODIS data by the International Geosphere-Biosphere Programme, IGBP (MCD12C1). In addition, the China Meteorological Forcing solar radiation dataset was downloaded from http://data.tpdc.ac.cn/en/data/ (Table 2). The solar radiation had a resolution of 0.1 degree and a 3-hour time step and was described in detail in (He et al., 2020; Yang et al., 2006, 2010) and Huang et al. (2017).

Table 2a Input data used in this study

Input data (2001-2018)				
Data source	**Data name**	**Used parameter**	**Time step**	**Spatial resolution**
MODIS Land Product	MOD11C1	Land Surface Temperature	daily	0.05 degree
http://data.tpdc.ac.cn/en/data/	MOD09CMG	Surface Reflectance	daily	0.05 degree
	MCD43C3	Albedo	daily	0.05 degree
	MOD13C1	NDVI	16-day	0.05 degree
	MCD12C1	Land cover	yearly	0.05 degree
China Meteorological Forcing Dataset	Srad	shortwave radiation	3-hourly	0.1degree
https://modis.gsfc.nasa.gov/data/				

Table 2b Data for verification

Flux tower	Lon. (°E)	Lat. (°N)	Altitude (m)	Land cover	Footprint (m)	Climate	Time period
Changbaishan	128.1	42.4	738	Forest	181 to 3070	Monsoon temperate continental climate	2003-2005
Qianyanzhou	115.06	26.74	102	Forest	120 to 1655	Subtropical monsoon climate	2003-2005
Dinghushan	112.53	23.17	240	Forest	129 to 1908	Monsoon humid climate	2003-2005
Yucheng	116.57	36.83	28	Cropland	16 to 190	Semi-humid monsoon climate	2003-2005
Haibei	101.32	37.62	3190	Grassland	19 to 195	Plateau continental climate	2003-2005
Neimeng	116.67	43.53	1200	Grassland	19 to 195	Temperate arid and semiarid continental climate	2004-2005
Dangxiong	91.07	30.5	4350	Grassland	27 to 163	Plateau monsoon climate	2004-2005
Wujiaqu	87.67	44.41	438	Grassland	400	Temperate arid and semiarid continental climate	2020.2.7-2020.12.17

3.2 Procedures for calculating satellite-based daily EF and ET

Figure 1 shows how to obtain the variable values to calculate the EF using the data described in section 3.1. The vegetation fraction, f_{veg} (Eq 13) was calculated with Eq. A1 in Appendix A based on the Normalized Difference Vegetation Index, NDVI, derived from the reflectance data in the MOD09CMG product (Eq. A2). When the daily reflectance data was not available, the MOD13C1 (measuring NDVI with a 16-day interval) was used as an auxiliary data source (Nishida et al., 2003). The actual available energy for the bare soil surface, Q_{soil} (Eq 13), was calculated by the radiation energy budget with the data of the MOD11C1 product using Eqs C1-C3 in Appendix C (Figure 1). The available energy for the vegetation Q_{veg} (Eq 13), was obtained by using the air temperature with Eq. C3 in Appendix C. The air temperature was

determined in Appendix F with the Nishada's Vegetation Index – temperature, VI-T_s diagram using the NDVI (MOD09CMG and MOD13C1), and the surface temperature tabulated in the MOD11C1 product with the diagram. The VI-T_s diagram was based on the assumption that dense vegetation has the minimum surface temperature and that dry, bare soil has the maximum temperature. Thus, there is a negative correlation between vegetation coverage and surface temperature. The calculation of the slope of the vegetation coverage, the surface temperature (also called the warm edge), and the intercept of them (also called the minimum surface temperature) is shown in Appendix F.

The instantaneous and daily equations were of the same form (Appendices D and E). The aerodynamic resistance of the bare soil, $r_{a\,soil}$ was determined with the equation D1 in appendix D originally proposed by Nishida (2003). The surface resistance of the bare soil, $r_{c\,soil}$ was found by subtracting the aerodynamic resistance of the bare soil from the total aerodynamic resistance (Eq. D2). The total aerodynamic resistance was computed with Eq. D3 (Griend and Owe, 1994 and Mu, 2007). The canopy surface resistance, $r_{c\,veg}$ was obtained with the method developed by Jarvis (1976, Eq. E1-E3 in Appendix E). The aerodynamic resistance of the forest cover was obtained with Eq. E4 and of both grassland and cropland with Eq. E5 (Kondo, 2000). The wind speed, which was input in Eqs E4 and E5, is given in Eq E6-E8. Then, the instantaneous and daily surface and aerodynamic resistance were computed with the equations provided in Appendices D and E using a combination of all available MODIS and Meteorological products as shown in Figure 1. Finally, these resistances were used to calculate the EF_{veg} in Eq. 5 and EF_{soil} in Eq. 6

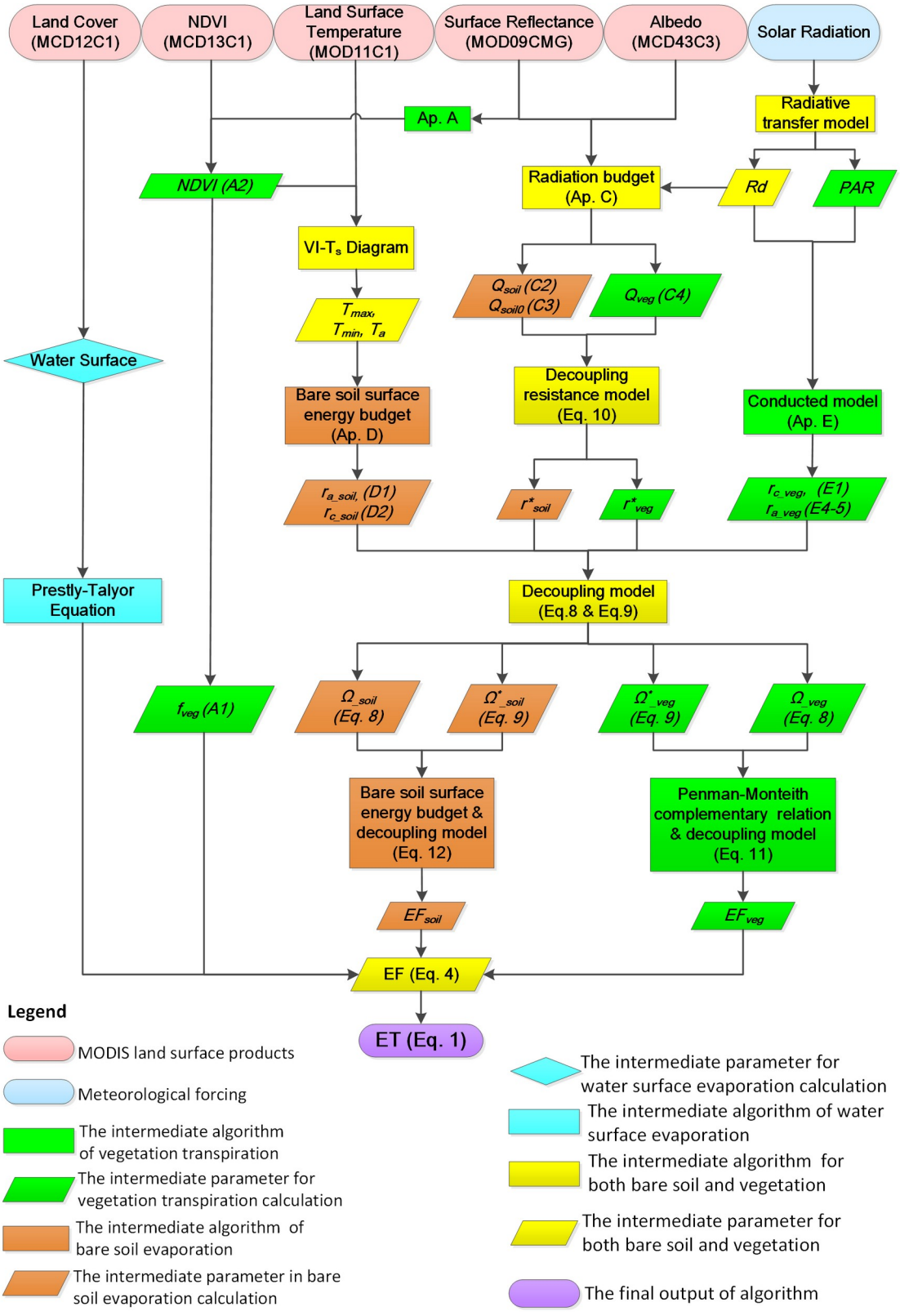

Figure 1: Schematic to calculate the evaporation fraction, EF (Eq. 13) and evaporation (Eq. 14). The ovals in the top row are the databases, and the square boxes are the algorithms, and parallelograms are the parameters. The numbers in the parenthesis are the equation to determine the parameters.

3.3 Data used for ground-truthing EF, ET and its components

The validity of the methods in Table 1 for calculating the actual ET was examined with data from seven flux towers from the Chinese FLUX Observation and Research Network (ChinaFlux): ChangBaiShan (CBS), QianYanZhou (QYZ), DingHuShan (DHS), YuCheng (YC), Haibei (HB), Neimeng (NM) and Dangxiong (DX) (Yu et al., 2006, 2008, 2013). These 7 flux towers are situated throughout China in different climate zones. CBS is in the monsoon temperate continental climate; QYZ and DHS are in the humid monsoon climate; YC is in the monsoon semi-humid climate; NM is in the temperate arid and semiarid continental climate; HB and DX sites are in the plateau continental climate, and land use, including forest, alpine, and grassland, as shown in Figure 2. The period considered was from 2003 to 2005 for CBS, QYZ, DHS, YC, and HB, and from 2004 to 2005 for the NM and DX sites. The sensible heat flux, latent heat flux, air temperature, and solar radiation observations are measured with a sampling frequency of 10 Hz with the open-path eddy covariance (3-D Sonic Anemometer of Campbell, and Li7500CO2/H2O analyzer of LI-COR) and standard meteorology equipment observations are aggregated every 30 minutes. The solar radiation, air temperature, and latent heat flux data at the closest 30-minute time interval to the MODIS Terra overpass time were used for instantaneous time scale validation. Daily temperatures were the average of the half-hour temperatures from 6:00 to 18:00. The Wujiaqu site is in the temperate arid and semiarid continental climate, and the measurement period was from Feb.7, 2020 to Dec. 17, 2020. The albedo measurements in the Wujiaqu site were used for diurnal albedo ground-truthing.

Several factors can cause discrepancies between satellite predicted *EF* and *ET* and flux tower measurements. These discrepancies may be due to the mismatch in the flux tower and the satellite footprint, the unsuitability of the satellite methods to the environmental conditions at the flux tower site (specifically high altitude sites with frozen soils and deserts), inaccuracies in the underlying assumptions of the theory, etc. We assumed the underlying assumptions were at fault when there was a

consistent difference for most flux towers. When the mismatch between our estimates and the flux tower measurements was for only a few of the flux towers, environmental factors and the particular site's footprint were likely the cause.

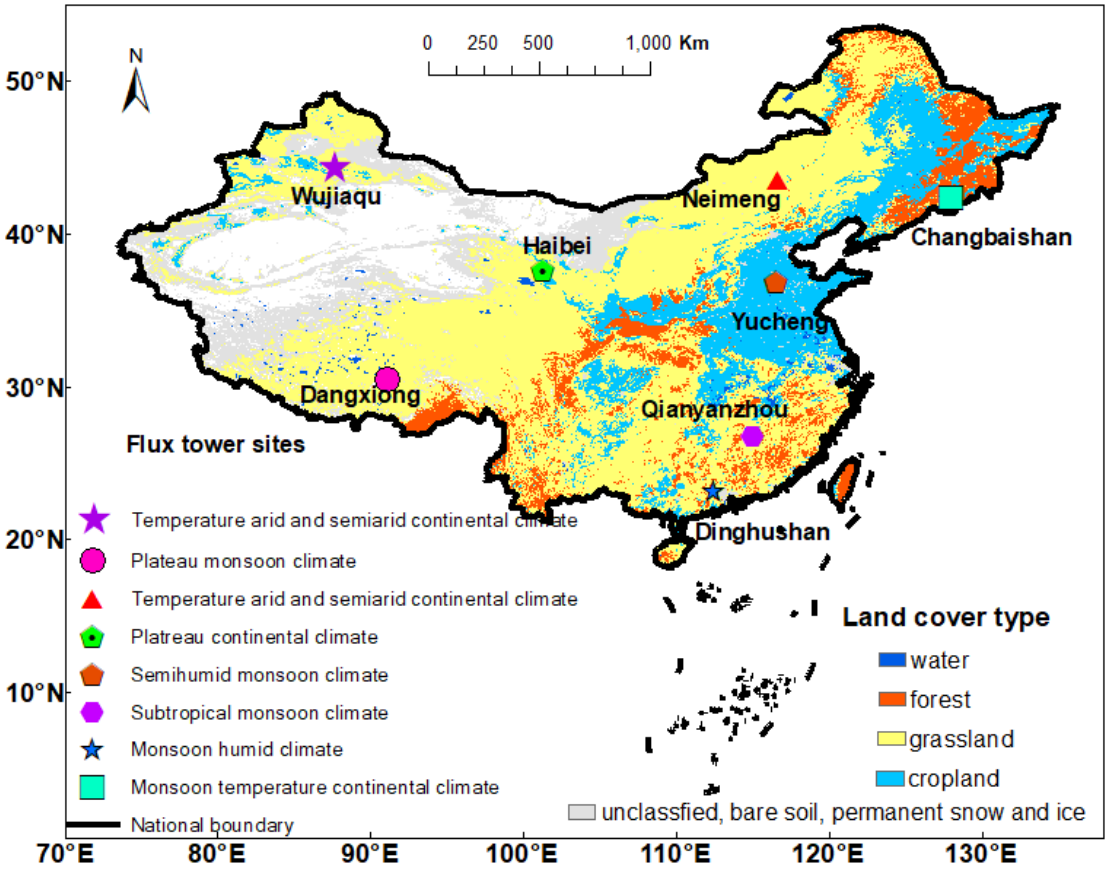

Figure 2. The location of the seven flux tower sites of the FLUX Observation and Research Network (ChinaFlux): ChangBaiShan (CBS), QianYanZhou (QYZ), DingHuShan (DHS), YuCheng (YC), Haibei (HB), Neimeng (NM), WuJiangQu (WJQ) and Dangxiong (DX). The 5 land cover types include water, forest, grassland, cropland, unclassified, bare soil, permanent snow, and ice, are shown in Figure 2.

3.4 Statistical methods

To compare the daily satellite evaporation (ET^{d}_{MOD}) calculation with the flux tower observed ET^{d}_{Obv}, the Pearson's correlation coefficient (r) and Root Mean Square Error (RMSE) were calculated.

$$r = \frac{\sum \left(ET^{d}_{MOD} - \overline{ET^{d}_{MOD}}\right)\left(ET^{d}_{Obv} - \overline{ET^{d}_{Obv}}\right)}{\sqrt{\sum ¿¿¿}} \quad (16)$$

r is the Pearson's correlation coefficient; ET^{d}_{MOD} is the satellite calculated evapotranspiration; $\overline{ET^{d}_{MOD}}$ is the average of ET^{d}_{MOD} ; ET^{d}_{Obv} is the observed evaporation with the flux towers; $\overline{ET^{d}_{Obv}}$ is the average of ET^{d}_{Obv}.

$$RMSE = \sqrt{\frac{\sum_{i=1}^{N}\left(ET^{d}_{MODi} - ET^{d}_{Obvi}\right)^2}{N}} \quad (17)$$

$RMSE$ is the Root Mean Square Error; N is the sample size.

4 Results

The input data, intermediate variables include the instantaneous and daily air, and final results calculated by the eight methods in Table 1 were compared with the seven flux tower measurements. The input data are instantaneous and daily download shortwave radiation data from China Meteorology Forcing Dataset (CMFD). The intermediate variables are the instantaneous and daily net radiation, air temperature, and daily evaporation fraction. The instantaneous and daily incoming shortwave radiation were previously compared with flux tower measurement by Huang et al. (2017) and is summarized in Section 4.1. Both instantaneous and daily net radiation and air temperature were ground-truthed with flux tower observations as detailed in Section 4.2 and 4.3. Finally, the daily evaporation fraction and evaporation were compared to that of the flux towers in Sections 4.4 and 4.5.

4.1 Incoming shortwave radiation

Huang et al. (2017) found that the R^2 of the instantaneous daily incoming shortwave radiation tabulated in the China Meteorological Forcing Datasets (CMFD) at that of the seven flux towers ranged from 0.30 to 0.73; the RMSE varied from 120.5 to 226.2 W m^{-1} (Figure H1 in Appendix H). The R^2 of total daily incoming

shortwave radiation ranged from 0.77 to 0.92, and RMSE varied between 27.1 and 40.4 W m^{-1} (Figure H2 in Appendix H). The discrepancy between the two measurement techniques was the largest for the Dinghushan(DHS), Haibei(HB), and Dangxiong(DX) sites. The observed incoming shortwave radiation for the DHS site located in southeast China with a monsoon climate was greater than that of the CMFD because the albedo was overestimated during the rainy phase (Huang et al., 2017). The HB and DX sites are both situated at high elevations. According to Yang et al. (2006), shortwave radiation was underestimated.

4.2 Net radiation

4.2.1 Instantaneously net radiation

The satellite-based model simulated instantaneous net radiation Rn^{i}_{MOD} was calculated by Eq C1 and C2 in Appendix C. In Figure 3, R^{i}_{i} shows a good agreement with the instantaneous net radiation for four of the seven flux towers at the time of the satellite overpass. This is consistent with the generally good fit of the instantaneous incoming shortwave radiation (Appendix H1). Although Rn^{i}_{MOD} are consistently underestimated in the CBS, QYZ, YCand NM four sites, it has satisfactory regression coefficients, R^2, ranging from 0.25 to 0.75, and root mean square error (RMSE) from 90.3 W m^{-2} to 158.4 W m^{-2} (Figure 3). Three remaining three sites (DHS, DX, and HB) perform poorly with RMSEs ranging from 103.1 to 198.9 W m^{-2}. The main reas on for the weak performance of these three sites are the inadequate quality of the downloaded incoming shortwave radiation in the CMFD data base (section 4.1, Appendix H1 and H2)

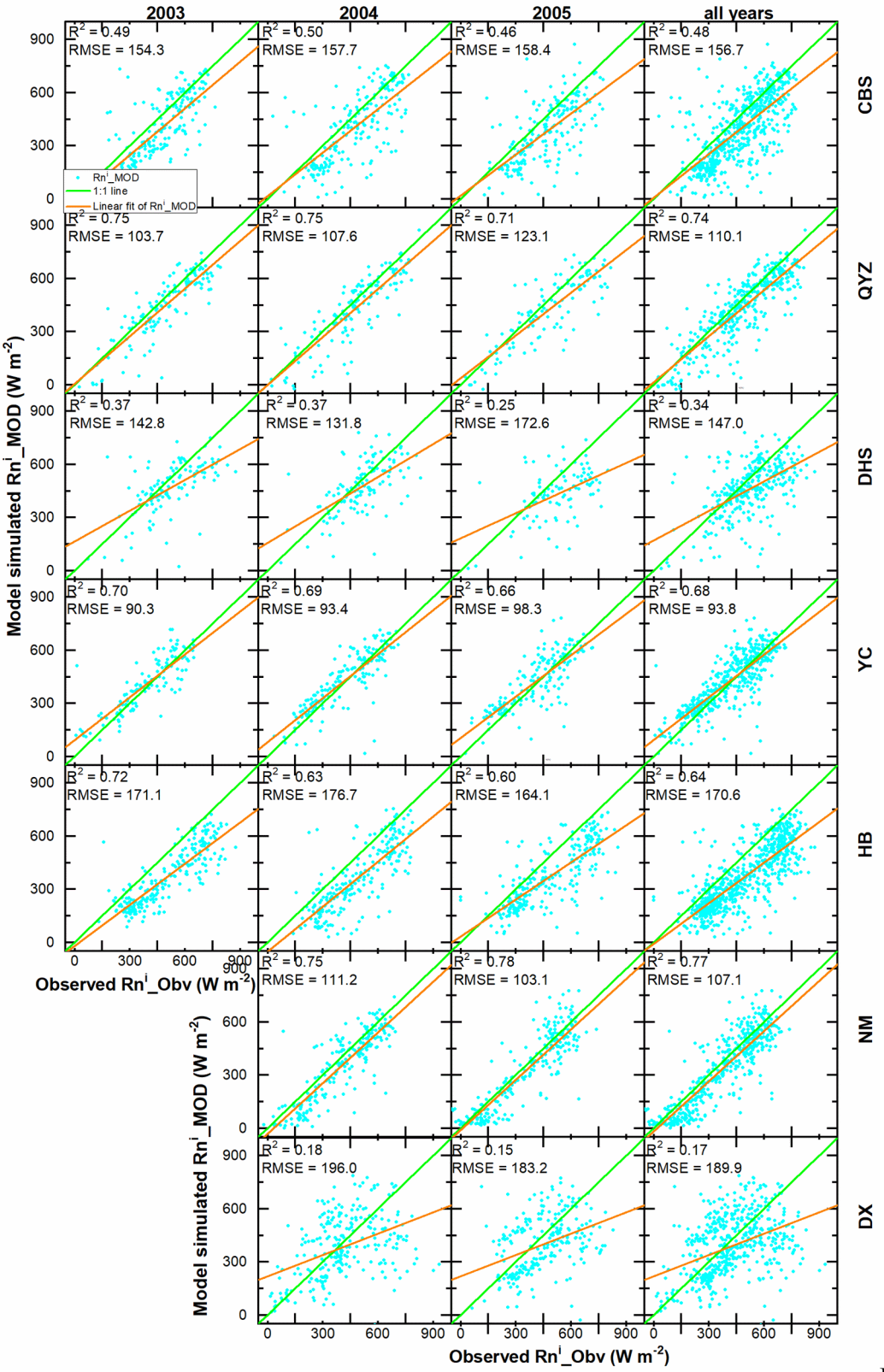

Figure 3. Scatter plots of satellite based model simulated instantaneous (during MODIS Terra overpass) net radiation Rn^{i}_{MOD} against flux tower observed instantaneous air temperature (Rn^{i}_{Obv}) in an individual year and entire period of 2003 to 2005 at

Changbaishan (CBS), Qianyanzhou (QYZ), Dinghushan (DHS), Yucheng (YC), Haibei (HB), Neimeng (NM) and Dangxiong (DX) sites.

4.2.2 Daily net radiation

The daily net radiation Rn^{d}_{MOD}, calculated by the equation C3 in the Appendix by assuming the longwave outgoing radiation term $\varepsilon\sigma T_s^4$ equals to the $\varepsilon\sigma T_a^4+4\varepsilon\sigma T_a^3(T_s-T_a)$ in Eq. C1. Rn^{d}_{MOD} is consistently overestimated the observed net radiation of the seven flux towers as shown in Figure 4, similar to that found by Tang et al. (2009) employed the same algorithms. Despite that the R^2 for most flux sites is good (R^2 ranges from 0.68 to 0.81) but the intercept with the y-axis is positive indicating a systematic error in the calculations. The daily net radiation for QYZ and DHS sites located in the south and southeast China (Figure 4) with a wet and warm climate with dense plant cover is relatively close. The daily net radiation for the other five sites (located in northern China, in colder, more arid, or semiarid climate) with less dense vegetation have a greater offset from the observed values. Especially, the DX site has the poorest fit R^2 of 0.29. We fist hypothesized that the systematic error causing the overestimation of the calculated satellite the net energy was related in part to the vegetation density through the longwave radiation term in Eq C1 in appendix C. Because we assumed that for daily scale, the longwave outgoing radiation term $\varepsilon\sigma T_s^4\approx\varepsilon\sigma T_a^4+4\varepsilon\sigma T_a^3(T_s-T_a)$ (Appendix C3), but we compared the $\varepsilon\sigma T_s^4$ and $\varepsilon\sigma T_a^4+4\varepsilon\sigma T_a^3(T_s-T_a)$, and found they are very close (the difference is lower than 1%). Then, we found that assuming the instantaneous albedo as its daily value may be the main reason. Studies (Cierniewski et al., 2015; Jääskeläinen & Manninen, 2021; Wang et al., 2015; Zhang et al., 2020) have shown that the albedo has a distinct diurnal variation and it has the minimum values during the noon time during the satellite overpass. Grant et al. found that the instantaneous albedo for a grass cover in

Australia was about 30% lower at noon than at 7 AM or 5 PM (Grant et al., 2000) as the diurnal albedo measurements of Wujiaqu site in Appendix I.

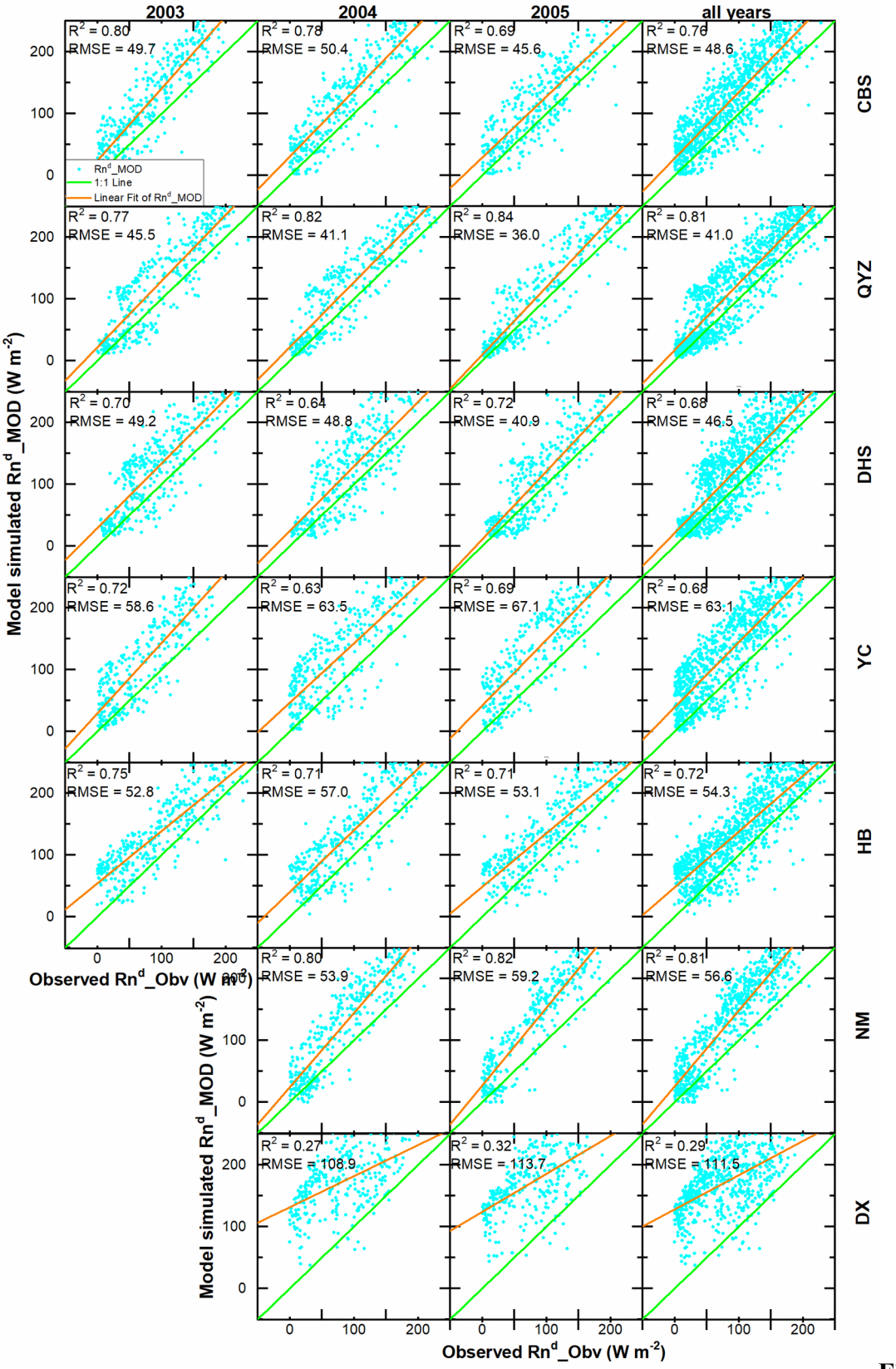

Fig

ure 4. Scatter plots of satellite-based model simulated daily net radiation (Rn^d_{MOD}) calculated with Eq. C1 plotted against the observed flux tower measurements (Rn^d _Obv) for an individual year and the entire 2003 to 2005 period. The abbreviation for the flux tower sites are in Figure 3, and the locations in Figure 1.

4.3 Air temperature

4.3.1 Instantaneous air temperature

Instantaneous air temperature $T_¿^i$ was calculated by the MODIS land surface data and NDVI data combined with the VI-Ts method in Appendix F. The comparison of the satellite-based instantaneous daytime air temperatures, $T_¿^i$ with the observed temperature $T_¿^i$ at the seven flux towers during the satellite overpass is shown in Figure 5. The predicted air temperature is in general agreement with the flux tower measurements with R^2 ranging from 0.50 to 0.84 and root mean square (RMSE) from 3.0 K to 15.9 K. The three sites Haibei, (HB), Neimeng (NM), and Dangxiong (DX) that are located at high elevations with an annual average of 0 ^{o}C and grass ground cover, deviated most (i.e., low R^2 and large RMSE). For these sites at high elevations, a distinct relationship between the NDVI and air temperature does not exist when the grass is frozen or snow-covered. Hence the underlying assumptions of the VI diagram (Appendix F) are violated and resulted in poor estimates of air temperature, as shown in Figure 5. When the NDVI has large spatial differences (e.g., forests in northeast China at the Changbaishan (CBS) site and cropland in North China Plain at the Yucheng (YC) site), the air temperature calculated with the VI-T_S diagram is comparable to the flux tower (Figure 5).

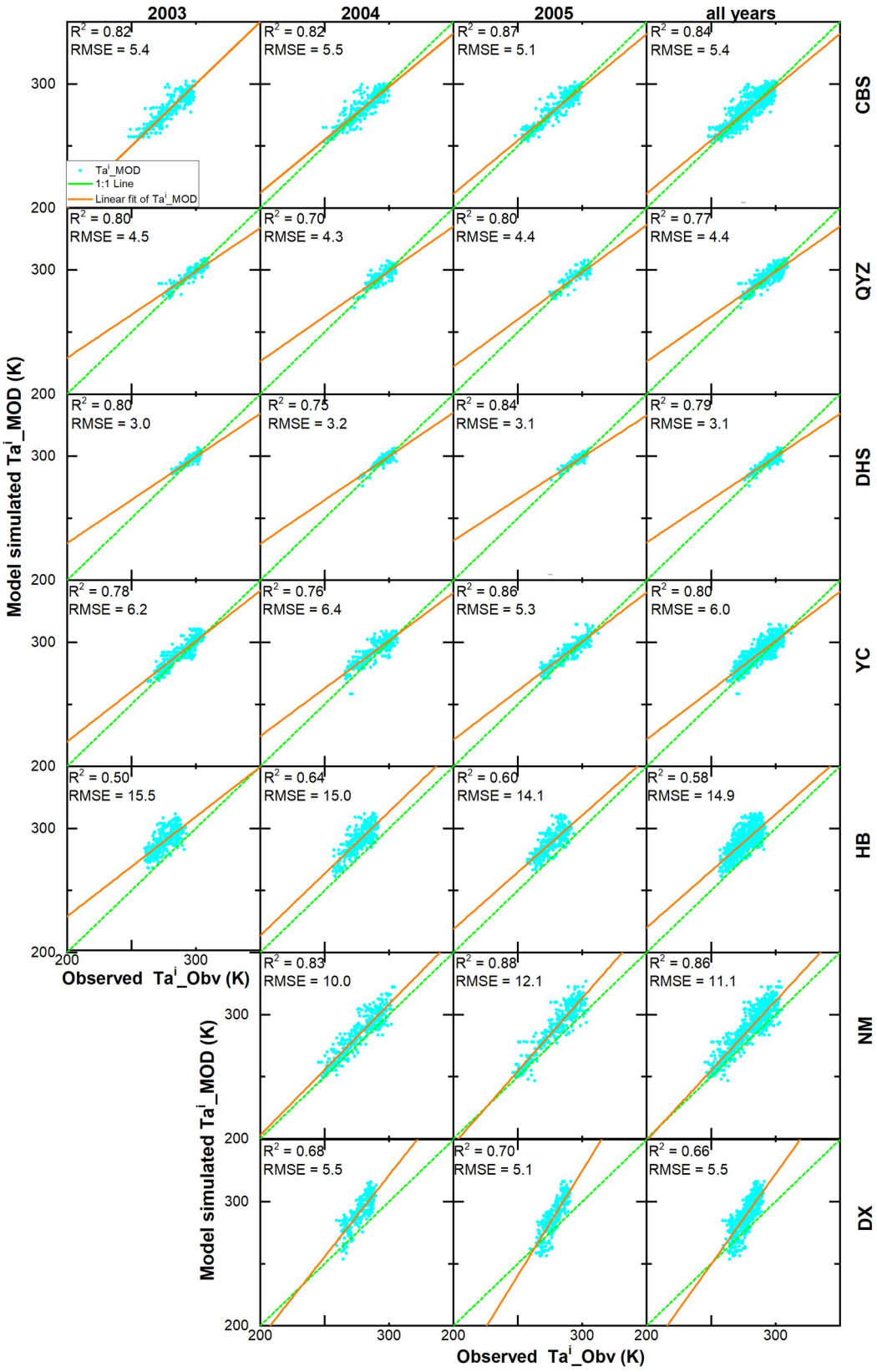

Figure 5. Scatter plots of satellite based model simulated instantaneous (during MODIS Terra overpass) air temperature Ta^i_{MOD} against flux tower observed instantaneous air temperature (Ta^i_{Obv}) in an individual year and entire period of 2003 to

2005. The flux tower abbreviations are in Figure 3, and the locations in Figure 1.

4.3.2 Daily air temperature

The model simulated daily mean air temperature, $T_{¿}^{d}$ was calculated by extending the daytime and nighttime instantaneous air temperature with a sine and cosine method in Appendix G. $T_{¿}^{d}$ was compared with the daily averaged air temperatures seven flux towers observations $T_{¿}^{d}$ in Figure 6. In general, the fit of the daily temperatures in Figure 6 is either equal or better than the instantaneous temperatures in Figure 5, with the R^2 ranging from 0.64 to 0.95 and RMSE ranging from 3.1 K to 6.4 K. Especially for the DX, NM, and HB sites, the fit is much better because 1) the random biases of flux tower measurements were reduced for the daily scale; 2) the calculation of the daily air temperature involved the nigh air temperature that was calculated by setting the satellite measured land surface temperature equal to the air temperature and did not involve the problems encountered with the VI-Ts diagram for these three sites (Appendix F). For the remaining four sites, the daily air temperatures based on the satellite measurements slightly underestimate the flux tower measurement (Figure 6). Therefore, the RMSE do not improve significantly over the instantaneous air temperatures in Figure 5.

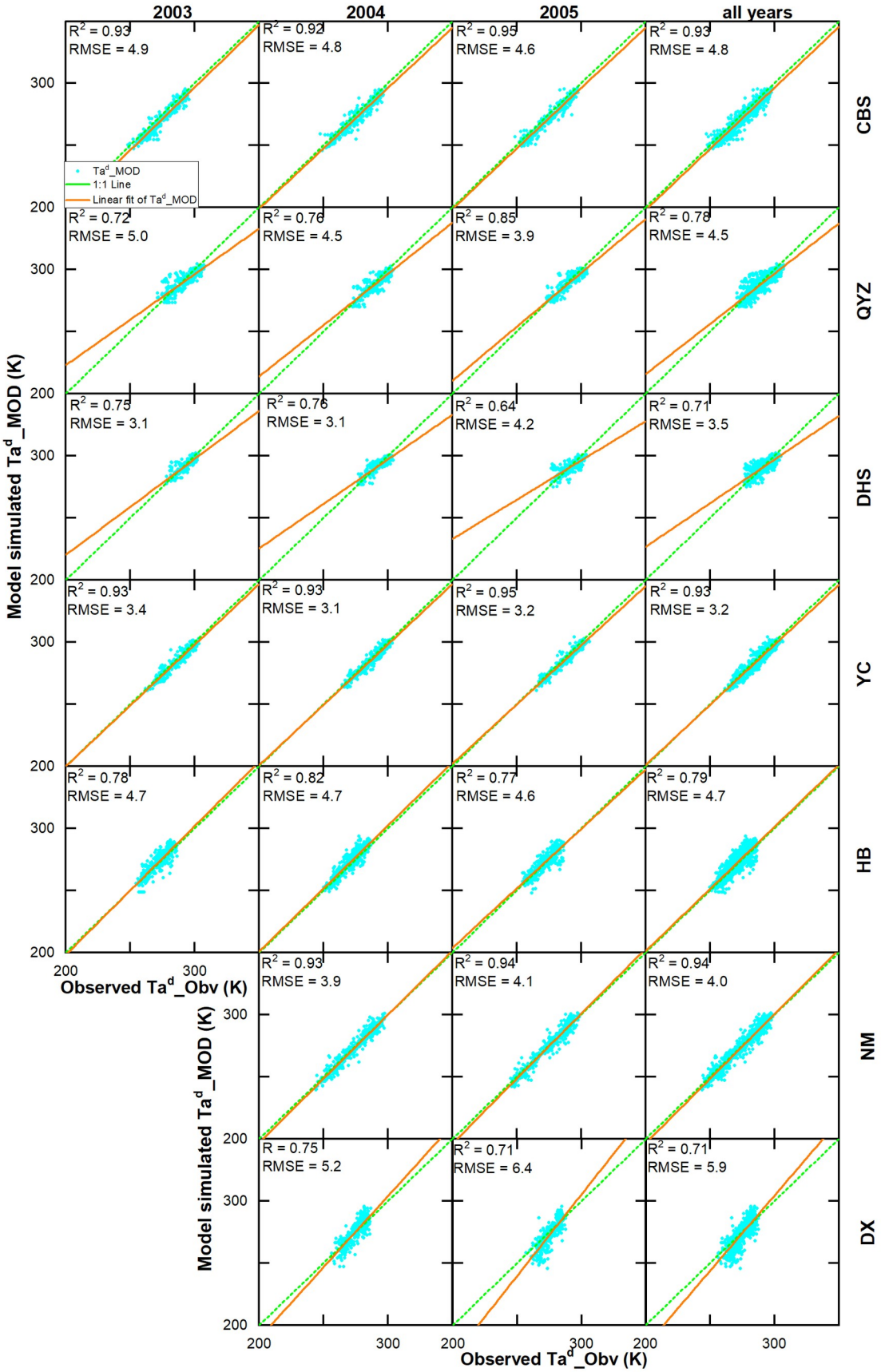

Figure 6. Scatter plots of satellite-based model simulated daily air temperature $T_{¿}^{d}$ against flux tower observed instantaneous air temperature ($T_{¿}^{d}$) in an individual year and entire period. Figures 1 and 3 give the location and abbreviations.

76

467 4.4 Evaporation fraction (EF)

468 The satellite-based evaporative fraction (EF) using the approximations in Table
469 1 for Eqs 12-15 was averaged over the observation period (Figure 7). As expected, the
470 greatest daily evaporation fractions are observed for the QYZ, DHS, and YC sites
471 which either have the highest rainfall or are irrigated and thus have ample water to
472 satisfy the evaporative demand (Figure 7). The other sites have limited rainfall, and
473 thus evaporation is less than the potential evaporation and consequently greater
474 amounts of incoming solar radiation converted into sensible heat. The calculated EF
475 values for the Dangxiong (DX) site in southwest China for all approximations in
476 Table 1 are much lower than the observed EF values (Table 3). The main reason is
477 the difference in vegetative cover for the flux tower's footprint and the grid cell on
478 which the satellite measurements. Sixty-five percent is vegetated in the flux tower
479 footprint, but only 13 % of the grid cell had vegetation. The DX site will therefore not
480 be considered further. The remaining EF values for the 6 flux tower sites are
481 averaged in Table 3.

482 The expressions of daily evaporation fractions in Table 1 can be divided into the
483 EFd method and the remaining methods consisting of EF0-EF7. For EFd, all daily
484 parameter and instantaneously parameter values were calculated, and for EF0-EF7,
485 one or more of the daily parameters were substituted for the instantaneous parameter
486 values. As can be seen in Table 3, when no substitutions were made, the daily
487 evaporation fraction, EF^d for tche EFd method resulted in a 50% underprediction of
488 the observed flux tower EF^d of 45%. The second group in which substitutions were

489 made of instantaneous values for daily parameters, EF0, in which the daily EF^d

490 equaled to the instantaneous EF^i during satellite overpass, performs relatively well
491 and provides a better estimate for the observed flux tower value than the EFd. For
492 EF1 in Table 3, the slope of the saturated vapor pressure for the day Δ^d was set equal
493 to the instantaneous value. The average value of EF1 for EF^d= 0.23 and is similar to
494 the EFd, which is half of the observed value. Next is the set of EF2-EF4 in which the

77
78

daily aerodynamic, surface and decoupling parameter resistances were replaced by their instantaneous values. None of the three approximation predict the observed EF^d very well (Table 3). Finally, the last set consists of EF5-EF7, in which the daily decoupling parameters were equated with the instantaneous values. Interestingly the EF^d values vary widely in this group and have the lowest performance for EF 5 with and an average value of EF^d=0.17 and the best performance for EF6 with EF^d=0.41. The latter is closer to the observed value of 0.45 than any other approximations, including the original method (EF0) proposed by Nishida and EFd that uses the complete equation (Eqs 11-14) without substitution Table 3.

The EF6 (as well as EF0 and EF7) method predicted the observed value EF^d value most accurately because in all the three methods the $\Omega^{¿d}$ was replaced by the instantaneous value $\Omega^{¿i}$ in some form (as can be seen from Table 1). Both $\Omega^{¿d}$ and $\Omega^{¿i}$ were calculated with Eq.10 in which either daily or instantaneous values were used of the following independent parameters: the slope of the saturated vapor pressure, the psychrometric constant, the aerodynamic resistance and $r^{¿}$. Considering these four independent parameters in Eq 10, we note that critical surface resistance $r^{¿}$ in Eq 11 is a function of the net radiation. As shown in Figure 4, the instantaneous net radiation is predicted much more accurately than the daily net radiation in Figure 5, which is overestimated by 20-40% using MODIS parameters. It means since the net radiation is the denominator in Eq 11, the instantaneous critical surface resistance $r^{¿i}$ is estimated relatively well, while the daily critical surface resistance $r^{¿d}$ is too small. In turn, this calculates $\Omega^{¿i}$ correctly and gives a too large $\Omega^{¿d}$, thus, the $\frac{\Omega_i^{¿}}{\Omega_d^{¿}}$ is too small.

In the calculation of the daily evaporation fraction, EF^d, in Eq 9, the $\frac{\Omega_i^{¿}}{\Omega_d^{¿}}$ term is in the denominator, and hence the EF^d is underestimated for all approximations (i.e., EF1-

EF5) that use the calculated $\frac{\Omega_i^{\iota}}{\Omega_d^{\iota}}$ value.

85

522 **Table 3.** The comparison of the flux tower observed daily mean evaporative fraction
523 (EF_Obv) and the satellite-based estimated EF with various methods (ET0-ET7
524 and ETd) during 2003 to 2005 at Changbaishan (CBS), Qianyanzhou (QYZ),
525 Dinghushan (DHS), Yucheng (YC), Haibei (HB), Neimeng (NM) and Dangxiong
526 (DX) sites.

Site	Observed	EF0	EF1	EF2	EF3	EF4	EF5	EF6	EF7	EFd
CBS	0.38	0.25	0.22	0.22	0.17	0.20	0.16	0.33	0.23	0.20
QYZ	0.63	0.53	0.39	0.39	0.41	0.34	0.34	0.57	0.50	0.38
DHS	0.60	0.52	0.35	0.34	0.37	0.33	0.21	0.81	0.49	0.33
YC	0.57	0.31	0.19	0.18	0.21	0.18	0.14	0.34	0.28	0.18
HB	0.28	0.20	0.10	0.10	0.08	0.08	0.05	0.21	0.15	0.08
NM	0.25	0.17	0.13	0.11	0.10	0.11	0.09	0.17	0.14	0.12
Average	**0.45**	**0.33**	**0.23**	**0.22**	**0.22**	**0.21**	**0.17**	**0.41**	**0.30**	**0.22**
DX	0.43	0.11	0.06	0.06	0.03	0.04	0.03	0.12	0.08	0.04

527

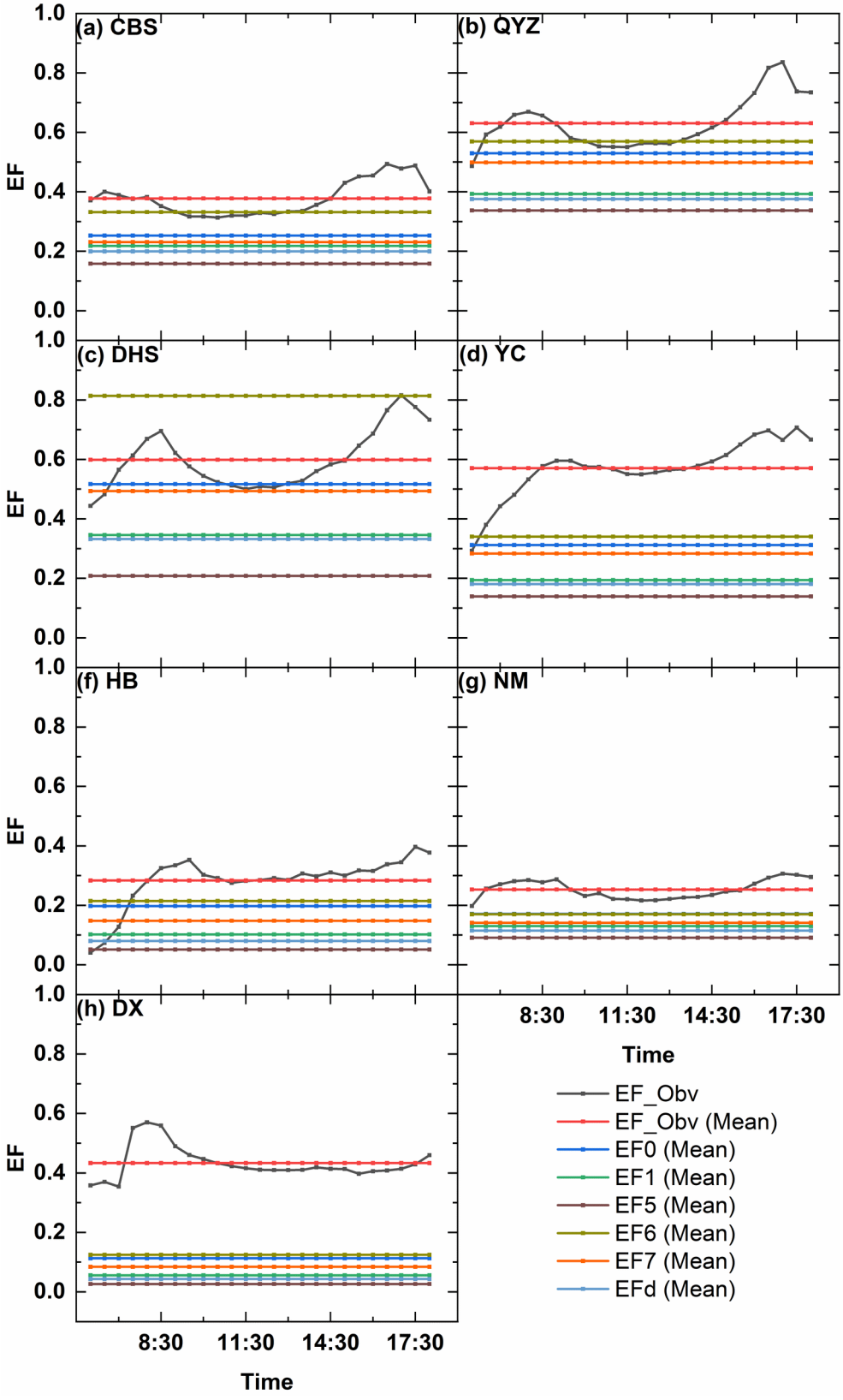

Figure 7. Comparison of multiyear averaged observed diurnal evaporation fraction, EF (EF_Obv) and estimated daily mean EF (EF0, EF1, EF2, EF3, EF4, EF5, EF6, EF7, and EFd) during 2003 to 2005 at Changbaishan (CBS), Qianyanzhou (QYZ), Dinghushan (DHS), Yucheng (YC), Haibei (HB), Neimeng (NM) and

Dangxiong (DX)

4.5 Evapotranspiration

The daily evapotranspiration calculated with the decoupling factor method (ET1 to ET7 and ETd in Table 1) is plotted against the flux tower measurements in Figure 8. The daily evaporation was obtained with Eq 15 by multiplying the evaporation fraction EF^d (Table 3) with the daily available energy, Q (Appendix C). In each plot in Figure 8, the daily evaporation calculated with the Nishida method (ET0 in Table 1) is also plotted for comparison. The averaged daily measured and calculated evaporation over the measurement period for each flux tower observation are shown in Table 4. Similar to the evaporation fraction depicted in Table 3, the satellite-based ET for Changbiashan, CBS (in the plot of (a)-(h) of Figure 8a), with the R^2 around 0.55 and RMSE 1.1 mm day^{-1} and Haibei, HB (in the plot of (i)-(p) of Figure 8b), with R^2 around 0.65 and RMSE 1.1 mm day^{-1} agree most closely with the flux tower measurements. The Dinghushan, DHS (in the plot of (q)-(x) of Figure 8a), with the R^2 around 0.25 and RMSE 1.5 mm day^{-1} and Dangxiong, DX (Figure 8c) with the R^2 around 0.35 and RMSE 1.5 mm day^{-1} deviate the farthest. Unlike the *EF* results in Table 3, ET0 predicted most closely the flux tower measurements with the greatest R^2, lowest RMSE (Figure 8a-8c, and Table 4). The ET6 method that most closely matched the observed EF^d value in Table 3 overpredicted the observed flux tower measurements significantly with RMSE 1.1 to 2.2 mm day^{-1} (Figure 8a-8c, and Table 4). Of the other methods that calculated the ET from the satellite data, ET1-ET4 underestimated the daily ET by nearly 50% and ET7 underestimated the daily ET by 30% (Table 4).

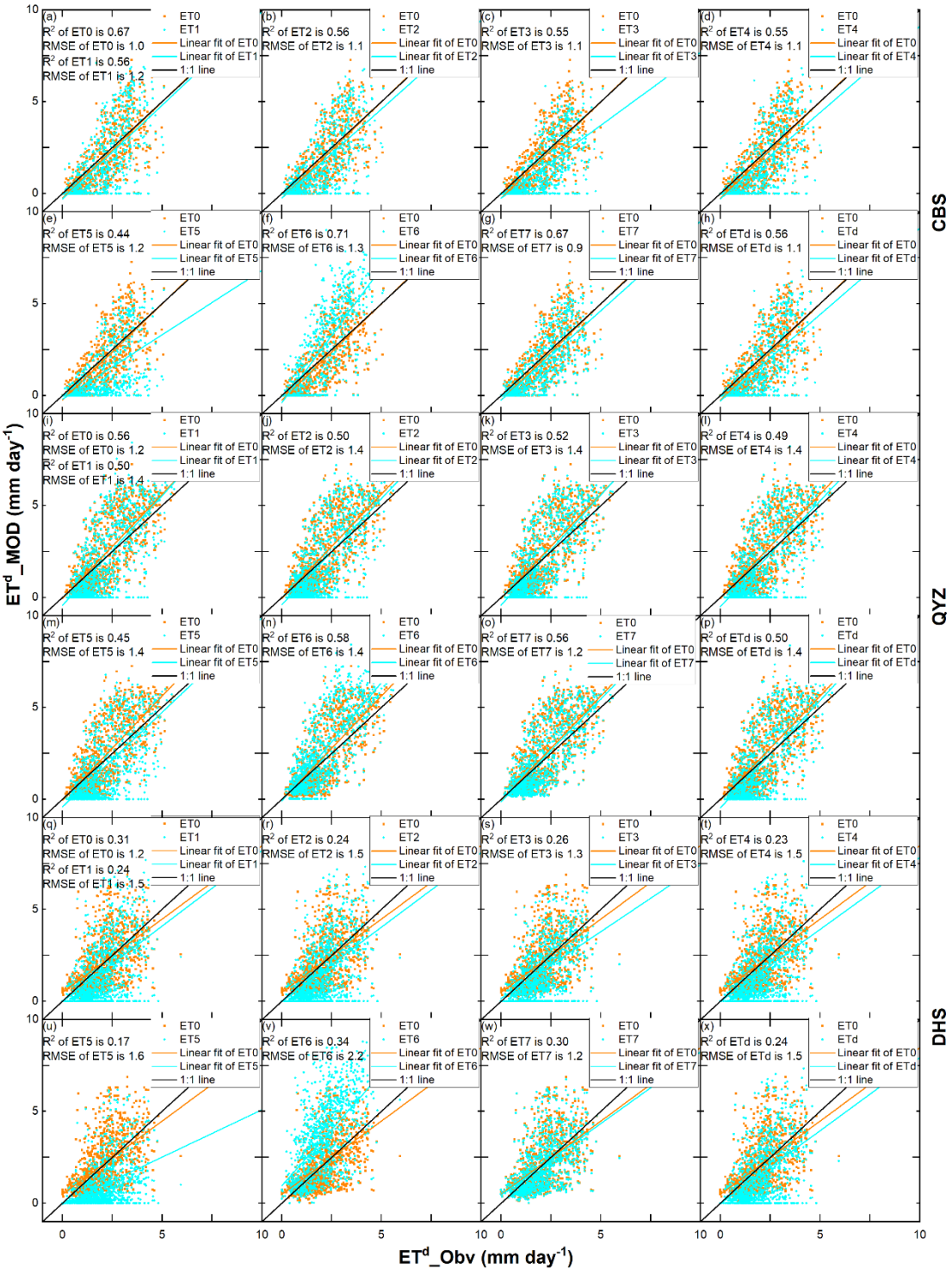

Figure 8a. Scatter plots of daily estimated ET data ET^{d}_MOD (ET0, ET1, ET2, ET3, ET4, ET5 ET6, ET7 and ETd) against flux tower daily observed ET data (ET^{d}_Obv) at entire period of 2003 to 2005 at Changbaishan (CBS), Qianyanzhou (QYZ), Dinghushan (DHS) sites.

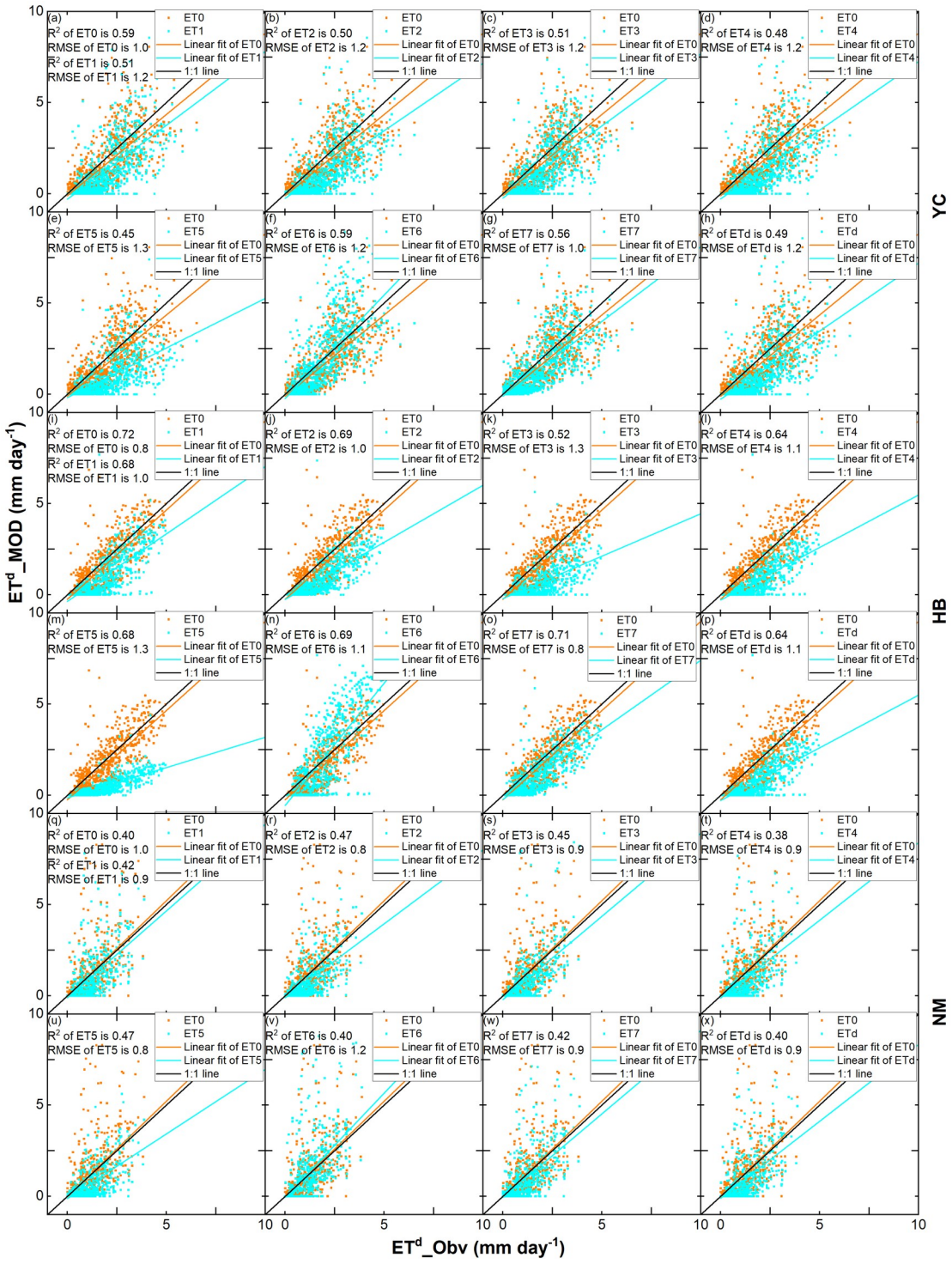

Figure 8b. Scatter plots of daily estimated ET data ETd_MOD (ET0, ET1, ET2, ET3, ET4, ET5 ET6, ET7 and ETd) against flux tower daily observed ET data (ETd_Obv) at entire period of 2003 to 2005 at Yucheng (YC), Haibei (HB) and 2004 to 2005 at Neimeng (NM) sites.

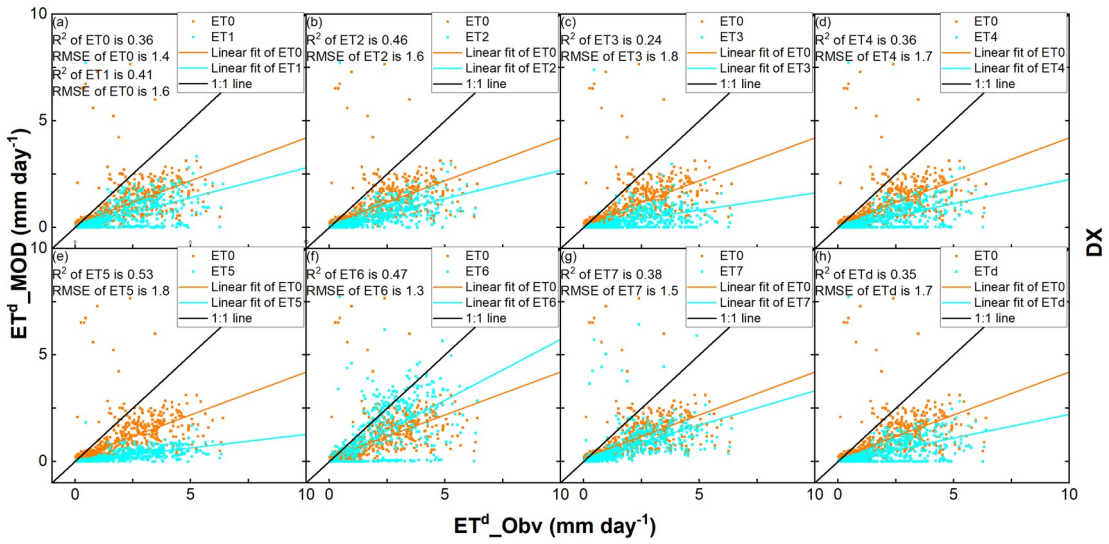

Figure 8c. Scatter plots of daily estimated ET data (ET0, ET1, ET2, ET3, ET4, ET5 ET6, ET7 and ETd) against flux tower daily observed ET data (ET_Obv) at entire period of 2004 to 2005 a) at Dangxiong (DX) site.

Table 4. The comparison of the flux tower observed daily mean ET (ET_Obv) and the satellite-based estimated ET with various methods (ET0-ET7 and ETd, ET6_new was calculated by the EF6 and the observed net radiation) during 2003 to 2005 at Changbaishan (CBS), Qianyanzhou (QYZ), Dinghushan (DHS), Yucheng (YC), Haibei (HB), Neimeng (NM) and Dangxiong (DX) sites.

Site	ET_Obv	ET0	ET1	ET2	ET3	ET4	ET5	ET6	ET7	ETd	ET6_new
						mm day^{-1}					
CBS	1.44	1.25	1.16	1.14	0.87	1.05	0.80	1.71	1.14	1.05	1.65
QYZ	2.05	2.27	2.01	1.97	2.03	1.86	1.70	2.55	2.16	1.93	2.35
DHS	2.06	2.13	1.68	1.65	1.65	1.61	0.99	3.47	2.05	1.61	3.24
YC	1.64	1.36	1.03	0.97	1.06	0.96	0.71	1.63	1.24	0.95	1.46
HB	1.37	1.09	0.65	0.60	0.43	0.50	0.31	1.28	0.82	0.51	1.18
NM	0.96	0.92	0.74	0.62	0.64	0.64	0.49	1.03	0.77	0.65	0.61
Average	1.59	1.50	1.21	1.16	1.11	1.10	0.83	1.95	1.36	1.12	1.75
DX	1.50	0.80	0.43	0.43	0.27	0.34	0.20	0.93	0.60	0.34	0.53

Considering the intermediate results in Fisections 4.1 to 4.4, the calculated *EF* with the method of Nashida (2003), EF0, was on the average 25% less than the observed flux tower *EF* (Figure 7 and Table 3). While the daily net radiation was 30% greater than the flux tower measurement (Figur 4). Thus, the daily ET0 was predicted more accurately than any other methods in Table 1. as it is the product of these two variables (Eq. 15) fortuitously provided the correct answer. Conversely, the EF6

method predicted the *EF* most closely to the flux tower measurements but overpredicted the daily evaporation, because of the 30% overestimates of the daily net radiation (Figur 4).

To reduce the impact of the overestimated daily net radiaiton on the daily *ET* estimates and examine whether the ET6 method would accurately predict the evaportation, we used EF6 method and the observed flux tower net radiation to recalculate the ET. The results are shown in Figure 9. The calculated ET generally match the observations with R^2 ranging from 0.27 to 0.67 and RMSE ranging from 0.9 to 1.4 mm day^{-1}. Compared to the ET0 method, the ET6 methad was generally more precise. For example, in the CBS site, the RMSE of ET6_new and ET0 is 0.9 mm day^{-1} and 1.0 mm day^{-1} respectively; in the QYZ site, the R^2 is 0.62 (ET6_new) and 0.56 (ET0), RMSE is 1.1 mm day^{-1} (ET6_new) and 1.2 mm day^{-1} (ET0); in the YC site, the R^2 is 0.49 (ET6_new) and 0.31(ET0), RMSE is 1.1 mm day^{-1} (ET6_new), and 1.2 mm day^{-1} (ET0); in the HB site, the R^2 is 0.63 (ET6_new) and 0.59 (ET0) respectively.

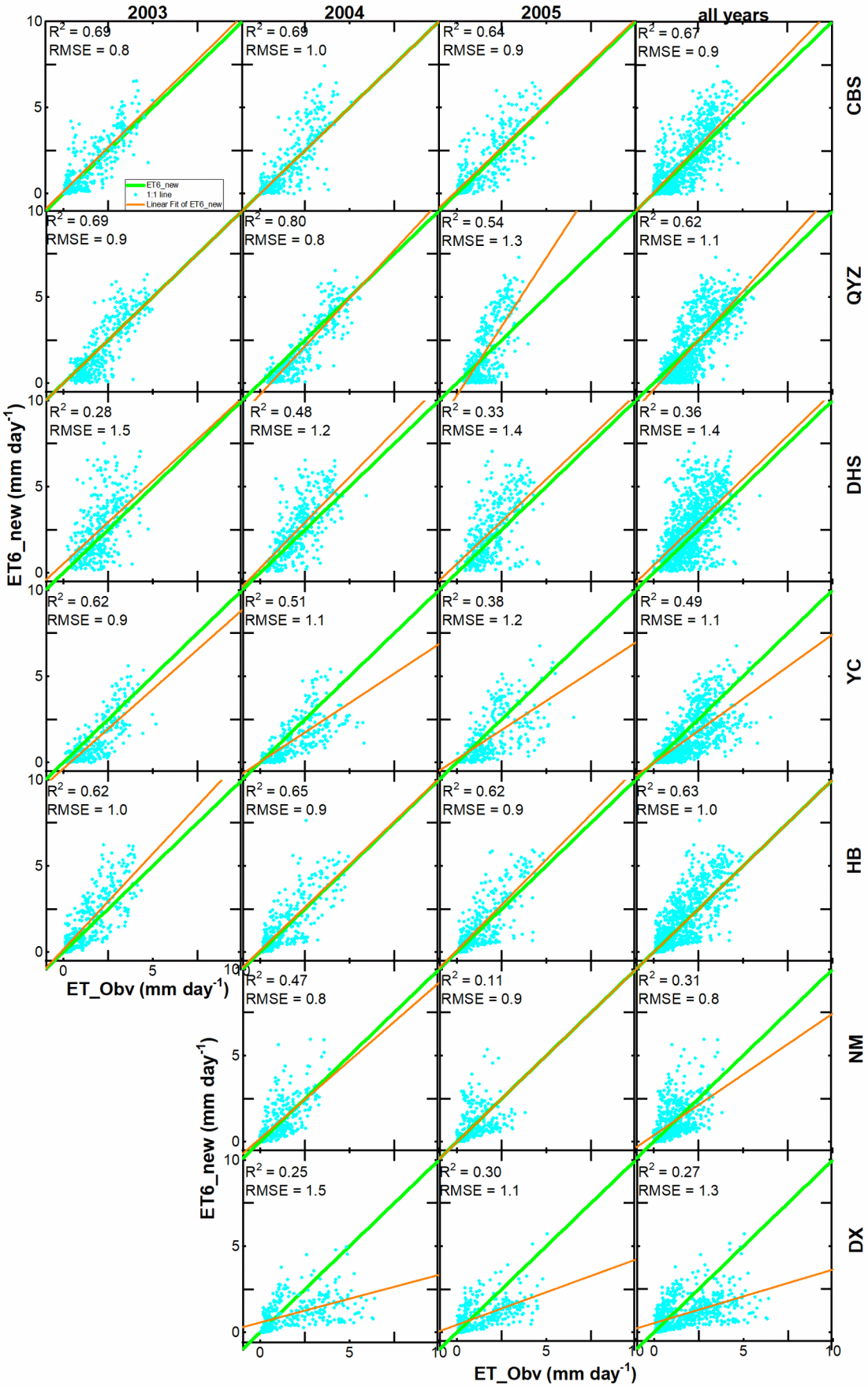

Figure 9. As Figure 3, but for daily estimated ET (ET6_new) which was based on the EF6 and observed net radiation against flux tower daily observed ET data

(ET_Obv).

5 Discussion and Conclusion

This study converted the instantaneous satellite observation into daily evaporation fraction and actual evapotranspiration, for forests, grassland, cropland, and deserts for large-scale applications in China. Our approach was based on the decoupling parameter method introduced by Tang & Li (2017) for irrigated winter wheat and summer maize cropland in the North China Plain. The decoupling parameter method is based on the relative contribution of radiative and aerodynamic terms to the overall evapotranspiration. We introduced eight different ways to calculate the daily evaporation from instantaneous satellite observation by replacing none, one, or several of the daily calculated intermediate variables by their instantaneous values (EFd, EF1-EF7 in Table 1). In this way, we were able to check the validity of the proposed conversions of instantaneous to daily values.

The MODIS 0.05-degree grid cell data, rather than the 250m or 500 m, was used as input because our focus was on determining the *ET* for China. A better agreement could have been obtained between flux tower measurement and satellite-based calculations of evaporation and its intermediate calculated values by calibrating the vegetation coverage (f_{veg}) in Eq. 2 using the same footprint MODIS data and flux tower surroundings. For example, for the DX site, the f_{veg} for the 0.05 grid cell is 0.13, and the f_{veg} for the flux tower footprint is 0.65. This resulted in a mismatch of satellite and flux tower evaporation. For this reason, the DX site was excluded from further consideration.

In evaluating the original Nishida method, we found that despite underestimating the evaporation fraction of the flux towers by 26% on average, the daily evaporation was more accurate than any of the eight methods based on the original Nishida method. The Nishida method assumed that the instantaneous evaporation was equal to the daily evaporation. By checking the intermediate values, we found that the daily net radiation was 30% too large. This too-large value with the 26% lower evaporation fraction made the daily *ET* estimates of the Nishada method came out well.

In calculating the daily net radiation, the dirnual albedo was assumed remained constant during the day. Studies (Cierniewski et al., 2015; Jääskeläinen & Manninen, 2021; Wang et al., 2015; Zhang et al., 2020) have proven that the albedo has a distinct diurnal variation with the minimum values during the noon when the satellite overpass (Grant et al., 2000). Observations at the Wujiaqu site (Appendix I) in Northweast China confirmed the findings. Thus, assuming that the albedo was constant resulted in the overestimation of the daily net radiation. It affected the intermediate calculated values such as the daily decoupling resistance $r^{¿d}$ in Eq. 11, where the daily net radiation is in the denominator. Other variables such as the daily decoupling parameter $\Omega^{¿d}$, depended on the value $r^{¿d}$ (Eq. 12). Utimalely the 30% error in the daily net radiation caused about 50% and 30% or higher underestimates of daily *EF* and *ET* respectively for six of the eight methods of the decoupling parameter method in Table 1.

Once we dropped the decoupling parameter $\Omega^{¿d}$ in determining the daily *EF* and used the correct daily net radiation, we found thet the Tang & Li (2017) method as adapted by us and provided both reasonable daily *EF* and *ET* estimates with the relative error of 8% and 9% respectively. Thus using the decoupling parameter method should be tried in other lacations as well for predicting the *ET* over large areas.

Acknowledgments

Funding for this research is provided by the The National Key Research and Development Program of China (NO.2017YFA0603703). The radiation dataset used in this study was developed by Ministry of Education Key Laboratory for Earth System Modeling, Department of Earth System Science, Tsinghua University and Center for Excellence in Tibetan Plateau Earth Sciences, Institute of Tibetan Plateau Research, Chinese Academy of Sciences. The flux tower data was provided by the Chinese FLUX Observation and Research Network. The authors declare no conflict of interest.

Appendix A: Vegetation fraction (f_{veg}) and Normalized Difference Vegetation Index (NDVI)

The vegetation fraction coverage (f_{veg}) is calculated as (Figure 1)

$$f_{veg} = \frac{NDVI - NDVI_{min}}{NDVI_{max} - NDVI_{min}} \quad \text{(A1)}$$

where the NDVI is the Normalized Difference Vegetation Index and can be calculated as:

$$NDVI = \frac{R_{nir} - R_{¿}}{R_{nir} + R_{¿}} \quad \text{(A2)}$$

where $NDVI_{min}$ is the NDVI of the bare soil without plants and $NDVI_{max}$ is the NDVI of the full vegetation cover, R_{nir} is the near-infrared reflectance and $R_{¿}$ is the red reflectance. The daily reflectance R_{nir} and $R_{¿}$ were measured by MODIS reflectance data MOD09CMG (Figure 1). Based on Tang (2009), we have set $NDVI_{min} = 0.22$ and $NDVI_{max} = 0.83$. Missing observation for the daily NDVI data was filled with the 16-day averaged NDVI values in the MOD13Q1data product (Fig. 1, Table 2).

Appendix B: The calculation of the slope of the saturated vapor, and the vapor pressure deficit of the air *VPD*

The slope of the saturated vapor (Δ),

$$\Delta = 4098 ¿¿ \quad \text{(B1)}$$

where T_a is the air temperature (°C) that can be calculated by the VI-Ts method in Appendix F with the NDVI and land surface data. VPD is the vapor pressure deficit of the air (kPa)

$$VPD = e^0(T_a) - e_a \quad \text{(B2)}$$

$$e^0(T_a) = 0.6108 \exp ¿ \quad \text{(B3)}$$

$$e_a = e^0(T_{dew}) \quad \text{(B4)}$$

$$e^0(T_{dew}) = 0.6108 \exp\left[\frac{17.27\,T_{dew}}{T_{dew}+237.3}\right] \quad \text{(B5)}$$

where the parenthesis indicates the independent variable, $e^0(T_a)$ is the saturation vapor pressure (kPa) at the air tempaerarue T_a (°C); e_a is the actual vapor pressure (kPa); $e^0(T_{dew})$ is the saturation vapor pressure (kPa) at the dew point temperature T_{dew} (°C). $T_{dew}$is set to the minimum air temperature during the day (°C) for the forest, water surface, and cropland. In arid areas like bare soil and non-irrigated grassland, T_{dew} maybe 2-3 °C lower than T_{min}. For this reason, 2 °C is subtracted from to the T_{min} in arid and semiarid areas to obtain the T_{dew}. Although these simplifications might introduce a bias in the final calculated *ET* value, our initial results showed that the effect was small.

Appendix C: Determining the net radiation (R_n), available energy of bare soil (Q_{soil}) and vegetation cover (Q_{veg}).

The net radiation was calculated by the land surface energy balance equation (Tang et al., 2009):

$$R_n = (1-albedo)R_d + \varepsilon\sigma(T_a-20)^4 - \varepsilon\sigma T_s^4 \quad \text{(C1)}$$

where *albedo* is obtained from the MODIS 16-day albedo data (MCD43C3); R_d is the 3-hourly incoming shortwave radiation from the China Meteorological Forcing Datasets (CMFD) (W m^{-2}) with a resolution of 0.1 degrees; ε is the emissivity from the MODIS daily surface temperature/emissivity data (MOD11C1); σ is the Stefan-Boltzmann constant 5.6704×10^{-8} W m^{-2} K^{-4}; T_a is the air temperature (K); T_S is the surface temperature (K); $\varepsilon\sigma(T_a-20)^4$ is the incoming long-wave radiation (W m^{-2}), $\varepsilon\sigma T_s^4$ is the upward long-wave radiation (W m^{-2}).

We follow Nishida (2003) to estimate the net radiation of vegetation R_{veg} (W m^{-2}) by assuming $T_s = T_a$

$$R_{veg} = (1-albedo)R_d + \varepsilon\sigma(T_a-20)^4 - \varepsilon\sigma T_a^4 \quad \text{(C2)}$$

And we estimate the net radiation of bare soil R_{soil} (W m^{-2}) following Nishida (2003), assuming $\varepsilon\sigma T_s^4 = \varepsilon\sigma T_a^4 + 4\varepsilon\sigma T_a^3(T_s-T_a)$

$$R_{soil} = (1-albedo)R_d + \varepsilon\sigma(T_a-20)^4 - \varepsilon\sigma T_a^4 - c\,4\varepsilon\sigma T_a^3(T_s-T_a) \quad \text{(C3)}$$

The available energy for the bare soil Q_{soil}(W m^{-2}), and for fully vegetated surfaces, Q_{veg}(W m^{-2}) and the maximum available energy for evaporation of bare soil, Q_{soil} (W m^{-2}) can be determined according to Nishida, (2003) as:

$$Q_{soil} \approx (1-C_G)(R_{n0} - 4\varepsilon\sigma T_a^3(T_{soil}-T_a)) \quad \text{(C4)}$$

$$Q_{veg} = R_{n0} \quad \text{(C5)}$$

where the C_G is an empirical coefficient ranging from 0.3 (wet soil) to 0.5 (dry soil) (Idso et al., 1975); R_{n0} is the net radiation assuming T_{soil} equals T_a (W m^{-2}); T_{soil} is the surface temperature of bare soil (K) calculated with the VI-Ts diagram (Appendix F)*;*

Appendix D: determining the aerodynamic and surface resistance of bare soil from satellite data

The aerodynamic resistance of the bare soil, $r_{a\,soil}$ (m s^{-1}), was calculated by Nishida, (2003), assuming that the maximum surface temperature of bare soil $T_{soil\,max}$ (K) occurs when the sum of latent heat flux and the sensible heat flux of the bare soil, namely, the available energy of bare soil Q_{soil}(W m^{-2}) is used as sensible heat flux and the latent heat flux is zero:

$$r_{a\,soil}=\frac{\rho C_p\left(T_{soil\,max}-T_a\right)}{Q_{soil}} \tag{D1}$$

$r_{a\,soil}$ is the aerodynamic resistance of the bare soil, (s m^{-1}), ρ is the air density, kg m^{-3}; C_p is the specific heat of the air, (J kg^{-1} K^{-1}); $T_{soil\,max}$ is the maximum surface temperature of bare soil (K), calculated by the VI-Ts method in Appendix F, T_a is the air temperature (K), $Q_{soil}$is the available energy of bare soil (W m^{-2}).

For the calculation of canopy surface resistance of bare soil $r_{c\,soil}$ (s m^{-1}), we follow the studies of Griend and Owe (1994), and Mu (2007):

$$r_{c\,soil}=r_{tot}-r_{a\,soil} \tag{D2}$$

$$r_{tot}=\frac{1.0}{\left(\frac{T_a}{293.15}\right)^{1.75}\frac{101300}{P}}*107.0 \tag{D3}$$

where r_{tot} is the total aerodynamic resistance (s m^{-1}); $r_{a\,soil}$ is the aerodynamic resistance over the bare soil (s m^{-1}); P is the atmospheric pressure (Pa), which was set to 101300 Pa.

Appendix E: Determining the surface resistance and aerodynamic of a vegetation canopy from satellite data

Jarvis (1976) found that the inverse of surface resistance of the canopy $\frac{1}{r_{c\,veg}}$ is equal to:

$$\frac{1}{r_{c\,veg}} = \frac{f_1(T_a) f_2(PAR) f_3(VPD) f_4(\varphi) f_5(co_2)}{r_{cMIN}} + \frac{1}{r_{cuticle}} \quad \text{(E1)}$$

where r_{cMIN} is the minimum resistance (s m^{-1}); r_{cMIN}= 33 (s m^{-1}) for cropland and r_{cMIN}=¿ 50 (s m^{-1}) for all other vegetation (Tang, 2009); $r_{cuticle}$is the canopy resistance related to diffusion through the cuticle layer of leaves (s m^{-1}). The value used in the Biome-BGC model is $r_{cuticle}$=100,000 (s m^{-1}, White et al., 2000), which is used by us.

The functions of air temperature T_a, $f_1(T_a)$ and photosynthetic active radiation *PAR*, $f_2(PAR)$ can be written as (Jarvis, 1975):

$$f_1(T_a) = \left(\frac{T_a - T_n}{T_o - T_n}\right)\left(\frac{T_x - T_a}{T_x - T_a}\right)^{\left(\frac{T_x - T_o}{T_o - T_n}\right)} \quad \text{(E2)}$$

where T_n, T_o and T_x are the minimum, optimal and maximum temperature for stomatal activity. According to Tang (2009), T_n=¿275.85 K, T_o=¿ 304.25 K and T_x = 318.45 K. The function $f_2(PAR)$ is expressed as:

$$f_2(PAR) = \frac{PAR}{PAR + A} \quad \text{(E3)}$$

where *PAR* is photosynthetic active radiation per unit area and time (μ mol m^{-2} s^{-1}) calculated by incoming solar radiation multiplied by 2.05 (Campbell and Norman, 2000); *A* is a parameter related to photon absorption efficiency at low light intensity, which was set to 152 μ mol m^{-2} s^{-1} (Tang, 2009); Nishida (2003) found that in Eq. E1 the following functions can be omitted without great loss of accuracy: the functions depending on vapor pressure deficit, $f_3(VPD)$, leaf water potential $f_4(\varphi)$ and carbon

dioxide vapor pressure, $f_5(CO_2)$.

Instantaneous and daily aerodynamic resistance of the canopy $r_{a\,veg}$ (s m^{-1}) is calculated by the empirical formulae of Kondo (2000) for forest cover, grassland, and cropland:

$$\frac{1}{r_{a\,veg(forest)}} = 0.008\,U_{50\,m} \quad \text{(E4)}$$

where $U_{50\,m}$ is the wind speed at 50 m height above the canopy (m s^{-1}) . The aerodynamic resistance grassland and cropland is Kondo (2000)

$$\frac{1}{r_{a\,veg(grassland\wedge cropland)}} = 0.003\,U_{1\,m} \quad \text{(E5)}$$

where $U_{1\,m}$ is the wind speed 1m above the canopy (m s^{-1}). The wind speed as a function of the height z, *U(z)* can be calculated by the logarithm profile of wind. As the $r_{a\,veg}$ has two variety calculation equations (E4 and E5) in the forest canopy (E4), grassland and cropland (E5), thus, we used the land cover classes from the yearly International Geosphere-Biosphere Programme (IGBP) (MCD12C1) to identify the land cover and choice the different equation of $r_{a\,veg}$. $U_{50\,m}$ and $U_{1\,m}$ were calculated by the logarithm profile of wind:

$$U(z) = U_{shear} \ln\left[\frac{(z-d)}{z_0}\right]/k \quad \text{(E6)}$$

where U_{shear} is the shear velocity (m s^{-1}); z is the height (m); d is the surface displacement (m); z_0 is the roughness length, we followed Kondo (2000), set as 0.005 m for bare soil and 0.01 m for grassland; k is the von Karman's constant and set as 0.4 following Nishida (2003). The shear velocity U_{shear} was calculated as:

$$U_{shear} = U_{1\,msoil}\frac{0.4}{\ln\left(\frac{1}{0.005}\right)}$$ where the $U_{1\,msoil}$ is the wind speed of bare soil at 1 m height (m s^{-1}), it was calculated as:

$$U_{1\,msoil} = 1/0.0015\,r_{a\,soil} \quad \text{(E7)}$$

The instantaneous air temperature can be calculated by the Vegetation Index-surface Temperature (VI-T_S) diagram (Nishida et al., 2003) using MODIS instantaneous surface temperature/emissivity data (MOD11C1) and daily calculated

NDVI as inputs (Appendix F).

Appendix F Calculating instantaneous air temperature based on the VI-Ts diagram

The calculation progress of instantaneous air temperature is shown in Appendix (a), the scatter plot of vegetation index (VI) versus land surface temperature (Ts) is drawn like Appendix (b). The slope of the warm edge can be calculated according to the slope and the maximum and minimum NDVI, by which, we can get the $T_{soil\,min}$ and $T_{soil\,max}$ as the intercept of the slope. At last, we assumed that the $T_{soil\,min}$ equals to the instantaneous air temperature T_a^i.

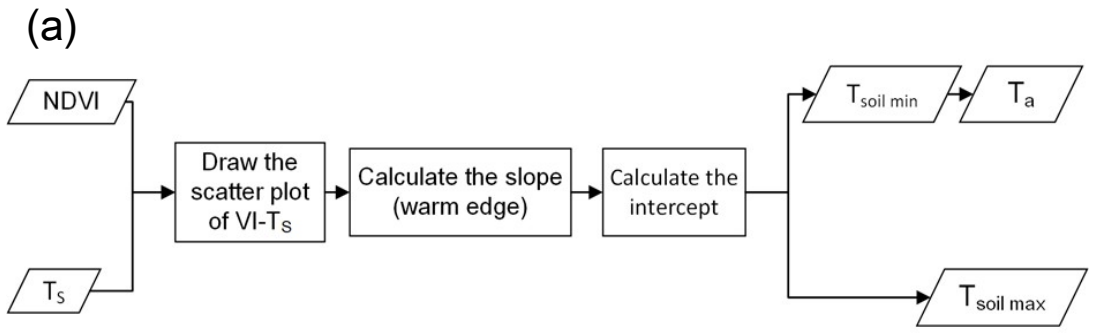

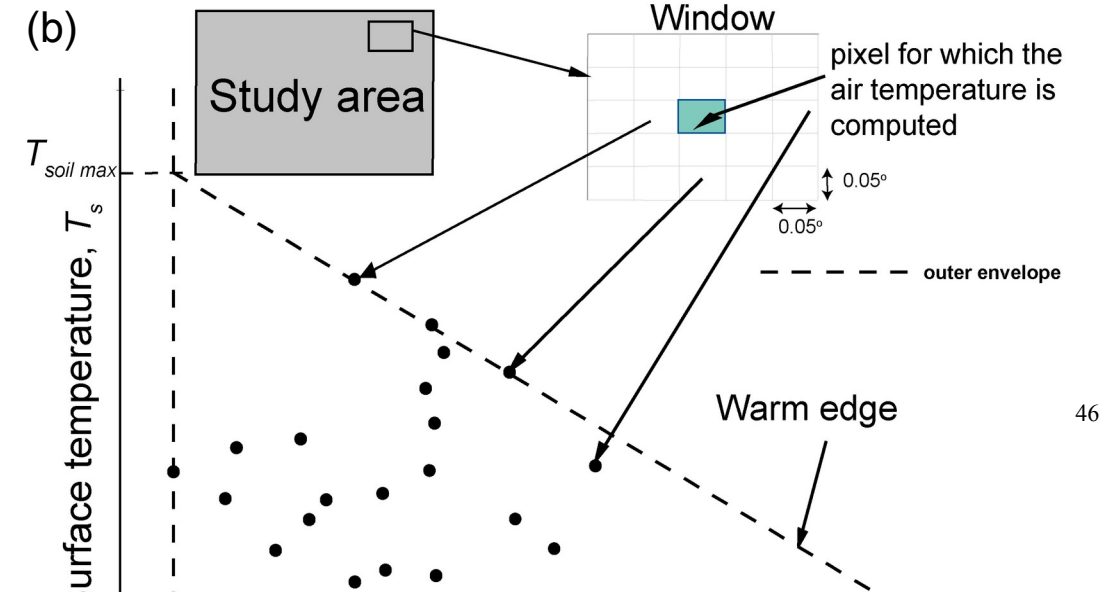

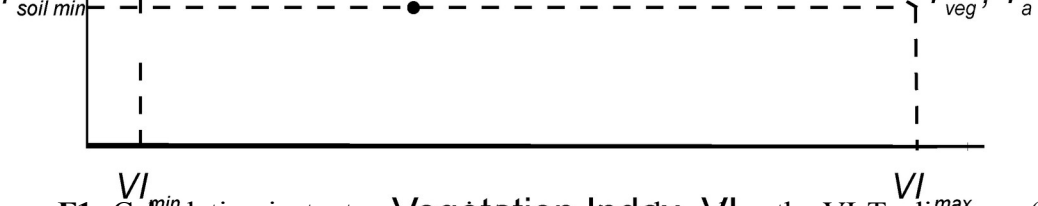

Figure F1: Calculating instantaneous air temperature based on the VI-Ts diagram. (a) is the calculation progress of the instantaneous air temperature and (b) is the scatter plot of the vegetation index and the surface temperature.

Appendix G. The flowchart daily air temperature of calculation

The daily mean air temperature T_a^d (K) was calculated as the average of 8 3-hourly air temperature estimates (Figure G1). These 3-hourly air temperature estimates were interpolated by the instantaneous air temperature $T_a^i$and the instantaneous night air temperature (which was assumed to be equal to the MODIS land surface temperature during the night) based on a sine-cosine fitting curve.

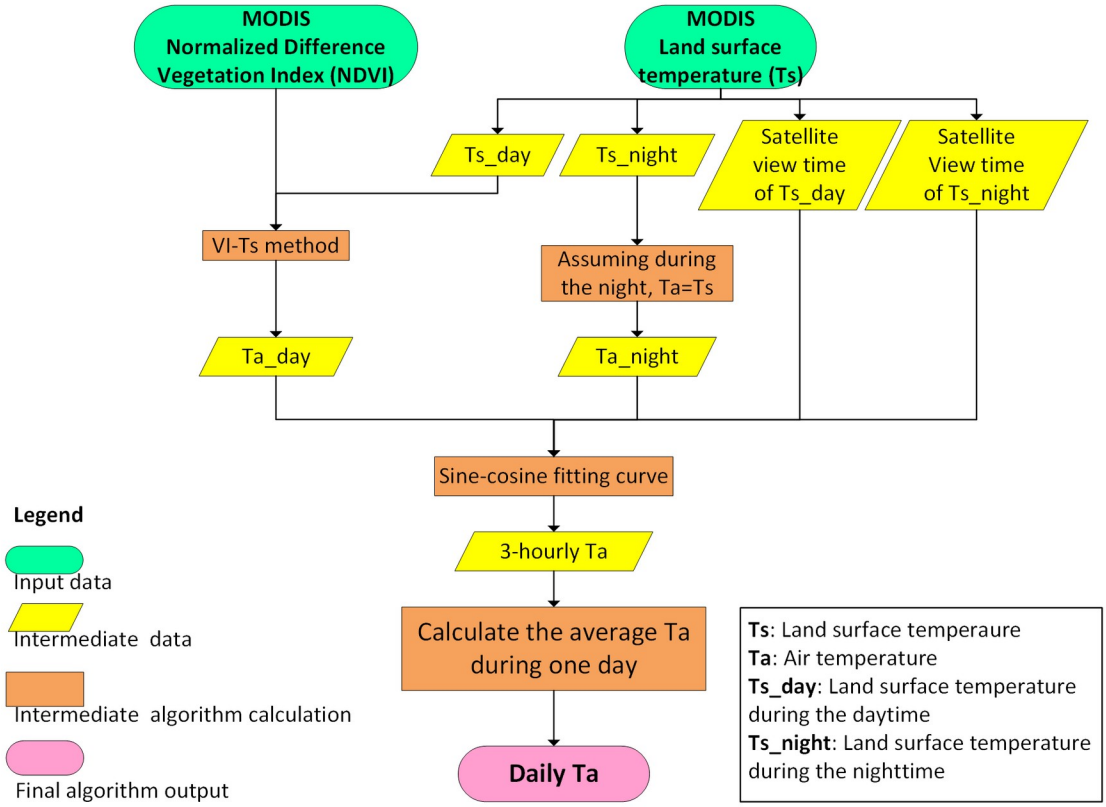

Figure G1: The flowchart daily air temperature of calculation.

Appendix H: shortwabe radiation validation

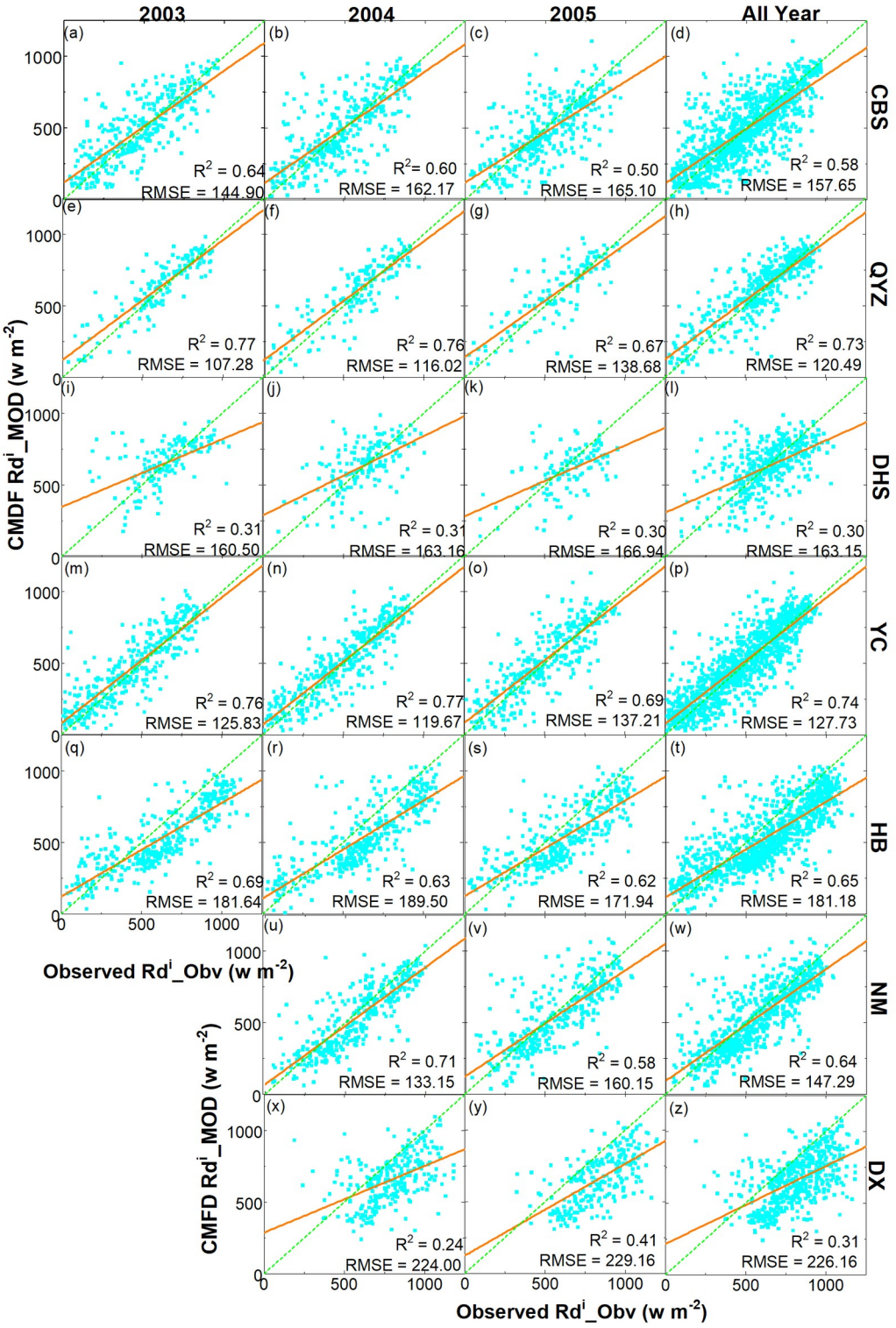

Figure H1. Instantaneous satellite-based shortwave radiation from the China Meteorolgy Forcing Dataset (CMFD), Rd^i_MOD against flux tower observed instantaneous download, shortwave radiation Rd^i_Obv. From https://www.spiedigitallibrary.org/journals/Journal-of-Applied-Remote-Sensing/volume-11/issue-02/026019/Evaluation-of-satellite-based-evapotranspiration-estimates-in-China/10.1117/1.JRS.11.026019.full. Reprinted with permission.

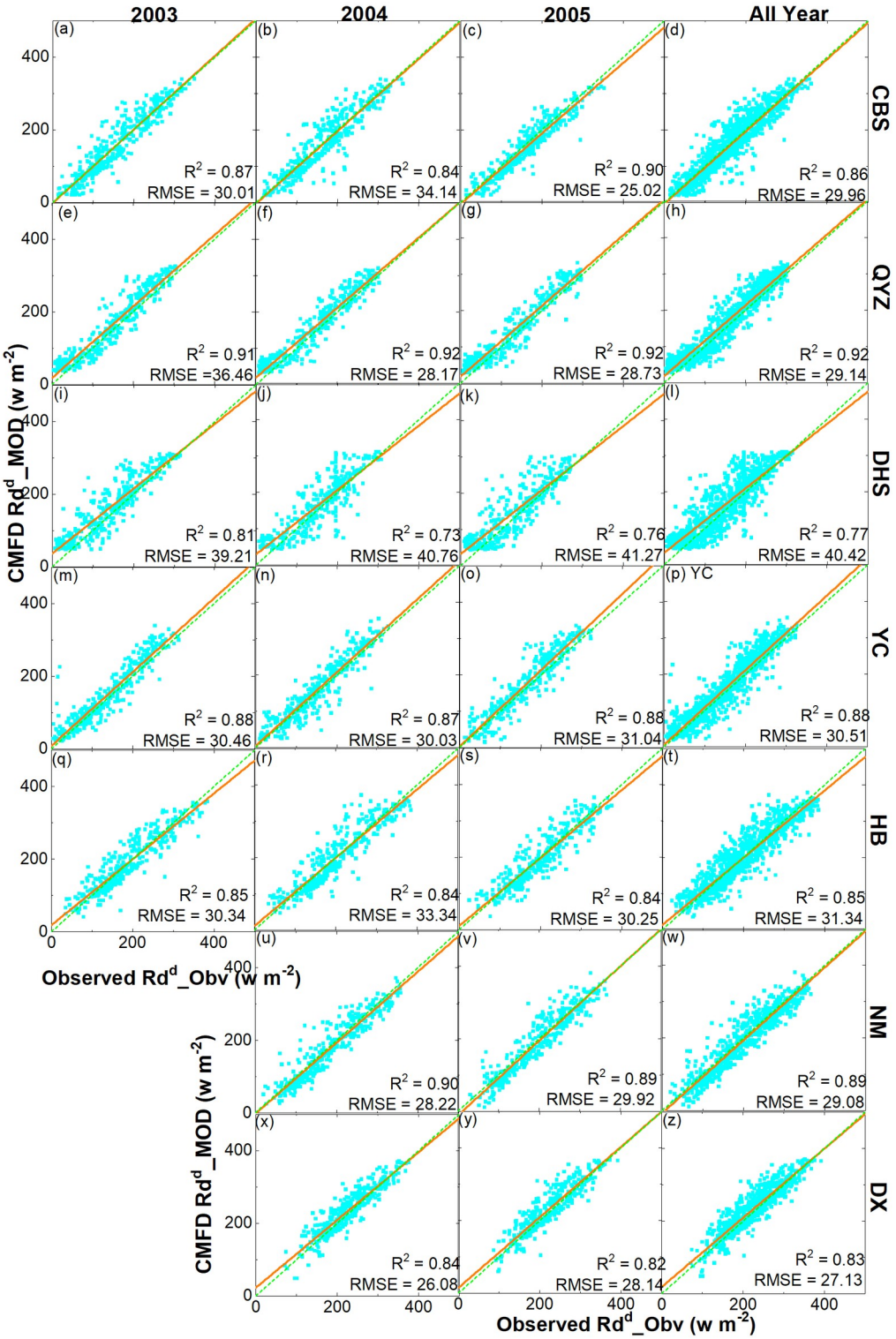

Figure H2 Daily mean download shortwave radiation from the China Meteorolgy Forcing Dataset (CMFD) Rd^d_MOD against flux tower observed daily mean download shortwave radiation (Rd^d_Obv). From https://www.spiedigitallibrary.org/journals/Journal-of-Applied-Remote-Sensing/volume-11/issue-02/026019/Evaluation-of-satellite-based-evapotranspiration-estimates-in-China/10.1117/1.JRS.11.026019.full. Reprinted with permission.

Appendix I: The diurnal variation of albedo

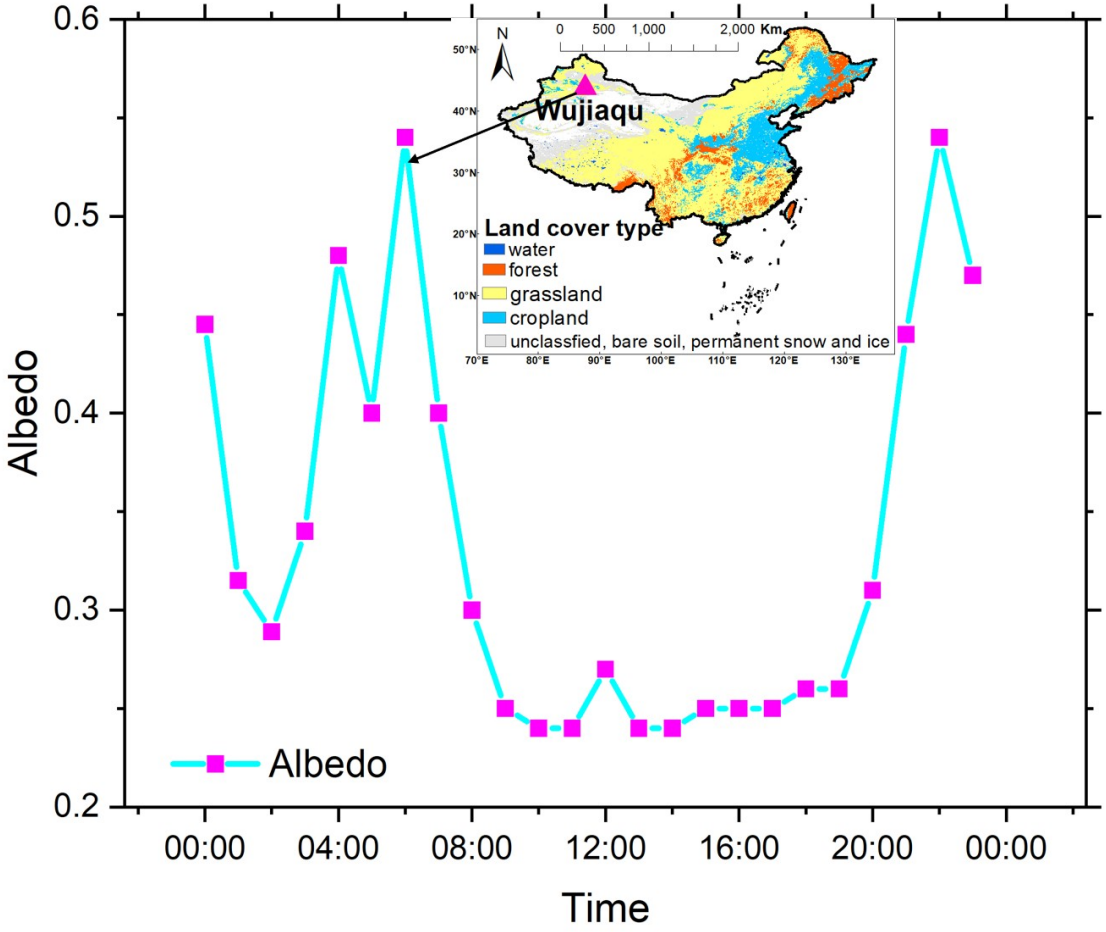

Figure I: The multimonth averaged observed diurnal albedo during Feb.2 to Dec.27 2020 at Wujiaqu flux tower site.

References

Ait Hssaine, B., Merlin, O., Ezzahar, J., Ojha, N., Er-Raki, S., & Khabba, S. (2020). An evapotranspiration model self-calibrated from remotely sensed surface soil moisture, land surface temperature and vegetation cover fraction: application to disaggregated SMOS and MODIS data. *Hydrology and Earth System Sciences*, *24*(4), 1781–1803. https://doi.org/10.5194/hess-24-1781-2020

Alfieri, J. G., Anderson, M. C., Kustas, W. P., & Cammalleri, C. (2017). Effect of the revisit interval and temporal upscaling methods on the accuracy of remotely sensed evapotranspiration estimates. *Hydrology and Earth System Sciences*, *21*(1), 83–98. https://doi.org/10.5194/hess-21-83-2017

Allen Richard G., Tasumi Masahiro, & Trezza Ricardo. (2007). Satellite-Based Energy Balance for Mapping Evapotranspiration with Internalized Calibration (METRIC)—Model. *Journal of Irrigation and Drainage Engineering*, *133*(4), 380–394.

https://doi.org/10.1061/(ASCE)0733-9437(2007)133:4(380)
Bastiaanssen, W. G. M., Menenti, M., Feddes, R. A., & Holtslag, A. A. M. (1998). A remote sensing surface energy balance algorithm for land (SEBAL). 1. Formulation. *Journal of Hydrology*, *212–213*, 198–212. https://doi.org/10.1016/S0022-1694(98)00253-4
Bastiaanssen, W. G. M., Pelgrum, H., Wang, J., Ma, Y., Moreno, J. F., Roerink, G. J., & van der Wal, T. (1998). A remote sensing surface energy balance algorithm for land (SEBAL).: Part 2: Validation. *Journal of Hydrology*, *212–213*, 213–229. https://doi.org/10.1016/S0022-1694(98)00254-6
Brutsaert, W., & Sugita, M. (1992). Application of self-preservation in the diurnal evolution of the surface energy budget to determine daily evaporation. *Journal of Geophysical Research: Atmospheres*, *97*(D17), 18377–18382. https://doi.org/10.1029/92JD00255
Brutsaert, W., Cheng, L., & Zhang, L. (2019). Spatial Distribution of Global Landscape Evaporation in the Early Twenty First Century by Means of a Generalized Complementary Approach. *Journal of Hydrometeorology*. https://doi.org/10.1175/JHM-D-19-0208.1
Cammalleri, C., Anderson, M. C., & Kustas, W. P. (2014). Upscaling of evapotranspiration fluxes from instantaneous to daytime scales for thermal remote sensing applications. *Hydrology and Earth System Sciences*, *18*(5), 1885–1894. https://doi.org/10.5194/hess-18-1885-2014
Chávez, J. L., Neale, C. M. U., Prueger, J. H., & Kustas, W. P. (2008). Daily evapotranspiration estimates from extrapolating instantaneous airborne remote sensing ET values. *Irrigation Science*, *27*(1), 67–81. https://doi.org/10.1007/s00271-008-0122-3
Chen, J. M., & Liu, J. (2020). Evolution of evapotranspiration models using thermal and shortwave remote sensing data. *Remote Sensing of Environment*, *237*, 111594. https://doi.org/10.1016/j.rse.2019.111594
Cierniewski, J., Karnieli, A., Kaźmierowski, C., Królewicz, S., Piekarczyk, J., Lewińska, K., et al. (2015). Effects of Soil Surface Irregularities on the Diurnal Variation of Soil Broadband Blue-Sky Albedo. *IEEE Journal of Selected Topics in Applied Earth Observations and Remote Sensing*, *8*(2), 493–502. https://doi.org/10.1109/JSTARS.2014.2330691
Cragoa, R., & Brutsaert, W. (1996). Daytime evaporation and the self-preservation of the evaporative fraction and the Bowen ratio. *Journal of Hydrology*, *178*(1), 241–255. https://doi.org/10.1016/0022-1694(95)02803-X
Delogu, E., Boulet, G., Olioso, A., Coudert, B., Chirouze, J., Ceschia, E., et al. (2012). Reconstruction of temporal variations of evapotranspiration using instantaneous estimates at the time of satellite overpass. *Hydrology and Earth System Sciences*, *16*(8), 2995–3010. https://doi.org/10.5194/hess-16-2995-2012
Dile, Y. T., Ayana, E. K., Worqlul, A. W., Xie, H., Srinivasan, R., Lefore, N., et al. (2020). Evaluating satellite-based evapotranspiration estimates for hydrological applications in data-scarce regions: A case in Ethiopia. *Science of The Total Environment*, *743*, 140702. https://doi.org/10c.1016/j.scitotenv.2020.140702
Faisol, A., Indarto, Novita, E., & Budiyono. (2020). An evaluation of MODIS global cevapotranspiration product (MOD16A2) as terrestrial evapotranspiration in East Java - Indonesia. *IOP Conference Series: Earth and Environmental Science*, *485*, 012002. https://doi.org/10.1088/1755-1315/485/1/012002
Gentine, P., Entekhabi, D., Chehbouni, A., Boulet, G., & Duchemin, B. (2007). Analysis of

evaporative fraction diurnal behaviour. *Agricultural and Forest Meteorology*, *143*(1), 13–29. https://doi.org/10.1016/j.agrformet.2006.11.002

Grant, I. F., Prata, A. J., & Cechet, R. P. (2000). The Impact of the Diurnal Variation of Albedo on the Remote Sensing of the Daily Mean Albedo of Grassland. *Journal of Applied Meteorology and Climatology*, *39*(2), 231–244. https://doi.org/10.1175/1520-0450(2000)039<0231:TIOTDV>2.0.CO;2

He, J., Yang, K., Tang, W., Lu, H., Qin, J., Chen, Y., & Li, X. (2020). The first high-resolution meteorological forcing dataset for land process studies over China. *Scientific Data*, *7*(1), 25. https://doi.org/10.1038/s41597-020-0369-y

Hou, M., Tian, F., Zhang, L., Li, S., Du, T., Huang, M., & Yuan, Y. (2019). Estimating Crop Transpiration of Soybean under Different Irrigation Treatments Using Thermal Infrared Remote Sensing Imagery. *Agronomy*, *9*(1), 8. https://doi.org/10.3390/agronomy9010008

Hu, X., Shi, L., Lin, L., & Zha, Y. (2019). Nonlinear boundaries of land surface temperature–vegetation index space to estimate water deficit index and evaporation fraction. *Agricultural and Forest Meteorology*, *279*, 107736. https://doi.org/10.1016/j.agrformet.2019.107736

Huang, L., Li, Z., Tang, Q., Zhang, X., Liu, X., & Cui, H. (2017). Evaluation of satellite-based evapotranspiration estimates in China. *Journal of Applied Remote Sensing*, *11*(2), 026019. https://doi.org/10.1117/1.JRS.11.026019

Jääskeläinen, E., & Manninen, T. (2021). The effect of snow at forest floor on boreal forest albedo diurnal and seasonal variation during the melting season. *Cold Regions Science and Technology*, *185*, 103249. https://doi.org/10.1016/j.coldregions.2021.103249

Jackson, R. D., Hatfield, J. L., Reginato, R. J., Idso, S. B., & Pinter, P. J. (1983). Estimation of daily evapotranspiration from one time-of-day measurements. *Agricultural Water Management*, *7*(1), 351–362. https://doi.org/10.1016/0378-3774(83)90095-1

Jung, M., Koirala, S., Weber, U., Ichii, K., Gans, F., Camps-Valls, G., et al. (2019). The FLUXCOM ensemble of global land-atmosphere energy fluxes. *Scientific Data*, *6*(1), 1–14. https://doi.org/10.1038/s41597-019-0076-8

Knipper, K. R., Kustas, W. P., Anderson, M. C., Nieto, H., Alfieri, J. G., Prueger, J. H., et al. (2020). Using high-spatiotemporal thermal satellite ET retrievals to monitor water use over California vineyards of different climate, vine variety and trellis design. *Agricultural Water Management*, *241*, 106361. https://doi.org/10.1016/j.agwat.2020.106361

Lhomme, J.-P., & Elguero, E. (1999). Examination of evaporative fraction diurnal behaviour using a soil-vegetation model coupled with a mixed-layer model. *Hydrology and Earth System Sciences*, *3*(2), 259–270. https://doi.org/10.5194/hess-3-259-1999

Li, S., Kang, S., Li, F., Zhang, L., & Zhang, B. (2008). Vineyard evaporative fraction based on eddy covariance in an arid desert region of Northwest China. *Agricultural Water Management*, *95*(8), 937–948. https://doi.org/10.1016/j.agwat.2008.03.005

Li, Z.-L., Tang, R., Wan, Z., Bi, Y., Zhou, C., Tang, B.-H., et al. (2009). A Review of Current Methodologies for Regional Evapotranspiration Estimation from Remotely Sensed Data. In *Sensors*. https://doi.org/10.3390/s90503801

Liu, X., Xu, J., Zhou, X., Wang, W., & Yang, S. (2020). Evaporative fraction and its application in estimating daily evapotranspiration of water-saving irrigated rice field. *Journal of Hydrology*, *584*, 124317. https://doi.org/10.1016/j.jhydrol.2019.124317

McNaughton, K. G., & Jarvis, P. G. (1983). Predicting effects of vegetation changes on transpiration and evaporation. *Water Deficits and Plant Growth*. Retrieved from http://agris.fao.org/agris-search/search.do?recordID=US201302611148

Minnis, P., Mayor, S., Smith, W. L., & Young, D. F. (1997). Asymmetry in the diurnal variation of surface albedo. *IEEE Transactions on Geoscience and Remote Sensing*, *35*(4), 879–890. https://doi.org/10.1109/36.602530

Miranda, R. de Q., Galvíncio, J. D., Moura, M. S. B. de, Jones, C. A., & Srinivasan, R. (2017, January 24). Reliability of MODIS Evapotranspiration Products for Heterogeneous Dry Forest: A Study Case of Caatinga [Research Article]. https://doi.org/10.1155/2017/9314801

Mu, Q., Heinsch, F. A., Zhao, M., & Running, S. W. (2007). Development of a global evapotranspiration algorithm based on MODIS and global meteorology data. *Remote Sensing of Environment*, *111*(4), 519–536. https://doi.org/10.1016/j.rse.2007.04.015

Mu, Q., Zhao, M., & Running, S. W. (2011). Improvements to a MODIS global terrestrial evapotranspiration algorithm. *Remote Sensing of Environment*, *115*(8), 1781–1800. https://doi.org/10.1016/j.rse.2011.02.019

Nichols, W. E., & Cuenca, R. H. (1993). Evaluation of the evaporative fraction for parameterization of the surface energy balance. *Water Resources Research*, *29*(11), 3681–3690. https://doi.org/10.1029/93WR01958

Nishida, K., Nemani, R. R., Running, S. W., & Glassy, J. M. (2003). An operational remote sensing algorithm of land surface evaporation. *Journal of Geophysical Research: Atmospheres*, *108*(D9). https://doi.org/10.1029/2002JD002062

Panwar, A., Renner, M., & Kleidon, A. (2020). Imprints of evaporative conditions and vegetation type in diurnal temperature variations. *Hydrology and Earth System Sciences*, *24*(10), 4923–4942. https://doi.org/10.5194/hess-24-4923-2020

Paul, S., Banerjee, C., & Nagesh Kumar, D. (2020). Evaluation Framework of Landsat 8–Based Actual Evapotranspiration Estimates in Data-Sparse Catchment. *Journal of Hydrologic Engineering*, *25*(9), 04020043. https://doi.org/10.1061/(ASCE)HE.1943-5584.0001992

Portela, M. M., Santos, J., & Studart, T. M. de C. (2019). Effect of the Evapotranspiration of Thornthwaite and of Penman-Monteith in the Estimation of Monthly Streamflows Based on a Monthly Water Balance Model. *Current Practice in Fluvial Geomorphology - Dynamics and Diversity*. https://doi.org/10.5772/intechopen.88441

Ryu, Y., Baldocchi, D. D., Black, T. A., Detto, M., Law, B. E., Leuning, R., et al. (2012). On the temporal upscaling of evapotranspiration from instantaneous remote sensing measurements to 8-day mean daily-sums. *Agricultural and Forest Meteorology*, *152*, 212–222. https://doi.org/10.1016/j.agrformet.2011.09.010

Shuttleworth, W. (1989). FIFE: The variation in energy partition at surface flux sites.

Sobrino, J. A., Gómez, M., Jiménez-Muñoz, J. C., & Olioso, A. (2007). Application of a simple algorithm to estimate daily evapotranspiration from NOAA–AVHRR images for the Iberian Peninsula. *Remote Sensing of Environment*, *110*(2), 139–148. https://doi.org/10.1016/j.rse.2007.02.017

Song, J. (1998). Diurnal asymmetry in surface albedo. *Agricultural and Forest Meteorology*, *92*(3), 181–189. https://doi.org/10.1016/S0168-1923(98)00095-1

Sugita, M., & Brutsaert, W. (1991). Daily evaporation over a region from lower boundary layer

profiles measured with radiosondes. *Water Resources Research*, *27*(5), 747–752. https://doi.org/10.1029/90WR02706

Tang, Q., Peterson, S., Cuenca, R. H., Hagimoto, Y., & Lettenmaier, D. P. (2009). Satellite-based near-real-time estimation of irrigated crop water consumption. *Journal of Geophysical Research: Atmospheres*, *114*(D5). https://doi.org/10.1029/2008JD010854

Tang, R., & Li, Z.-L. (2017). An improved constant evaporative fraction method for estimating daily evapotranspiration from remotely sensed instantaneous observations. *Geophysical Research Letters*, *44*(5), 2319–2326. https://doi.org/10.1002/2017GL072621

Tang, R., Li, Z.-L., & Sun, X. (2013). Temporal upscaling of instantaneous evapotranspiration: An intercomparison of four methods using eddy covariance measurements and MODIS data. *Remote Sensing of Environment*, *138*, 102–118. https://doi.org/10.1016/j.rse.2013.07.001

Tang, R., Li, Z.-L., Sun, X., & Bi, Y. (2017). Temporal upscaling of instantaneous evapotranspiration on clear-sky days using the constant reference evaporative fraction method with fixed or variable surface resistances at two cropland sites. *Journal of Geophysical Research: Atmospheres*, *122*(2), 784–801. https://doi.org/10.1002/2016JD025975

Van Niel, T. G., McVicar, T. R., Roderick, M. L., van Dijk, A. I. J. M., Beringer, J., Hutley, L. B., & van Gorsel, E. (2012). Upscaling latent heat flux for thermal remote sensing studies: Comparison of alternative approaches and correction of bias. *Journal of Hydrology*, *468–469*, 35–46. https://doi.org/10.1016/j.jhydrol.2012.08.005

Wang, D., Liang, S., He, T., Yu, Y., Schaaf, C., & Wang, Z. (2015). Estimating daily mean land surface albedo from MODIS data. *Journal of Geophysical Research: Atmospheres*, *120*(10), 4825–4841. https://doi.org/10.1002/2015JD023178

Wang, K., & Dickinson, R. E. (2012). A review of global terrestrial evapotranspiration: Observation, modeling, climatology, and climatic variability. *Reviews of Geophysics*, *50*(2). https://doi.org/10.1029/2011RG000373

Yang, K., Koike, T., & Ye, B. (2006). Improving estimation of hourly, daily, and monthly solar radiation by importing global data sets. *Agricultural and Forest Meteorology*, *137*(1), 43–55. https://doi.org/10.1016/j.agrformet.2006.02.001

Yang, K., He, J., Tang, W., Qin, J., & Cheng, C. C. K. (2010). On downward shortwave and longwave radiations over high altitude regions: Observation and modeling in the Tibetan Plateau. *Agricultural and Forest Meteorology*, *150*(1), 38–46. https://doi.org/10.1016/j.agrformet.2009.08.004

Zhang, K., Kimball, J. S., Mu, Q., Jones, L. A., Goetz, S. J., & Running, S. W. (2009). Satellite based analysis of northern ET trends and associated changes in the regional water balance from 1983 to 2005. *Journal of Hydrology*, *379*(1), 92–110. https://doi.org/10.1016/j.jhydrol.2009.09.047

Zhang, K., Kimball, J. S., Nemani, R. R., & Running, S. W. (2010). A continuous satellite-derived global record of land surface evapotranspiration from 1983 to 2006. *Water Resources Research*, *46*(9). https://doi.org/10.1029/2009WR008800

Zhang, L., & Lemeur, R. (1995). Evaluation of daily evapotranspiration estimates from instantaneous measurements. *Agricultural and Forest Meteorology*, *74*(1), 139–154. https://doi.org/10.1016/0168-1923(94)02181-I

Zhang, X., Jiao, Z., Dong, Y., He, T., Ding, A., Yin, S., et al. (2020). Development of the Direct-

Estimation Albedo Algorithm for Snow-Free Landsat TM Albedo Retrievals Using Field Flux Measurements. *IEEE Transactions on Geoscience and Remote Sensing*, *58*(3), 1550–1567. https://doi.org/10.1109/TGRS.2019.2946598

Zou, M., Zhong, L., Ma, Y., Hu, Y., Huang, Z., Xu, K., & Feng, L. (2018). Comparison of Two Satellite-Based Evapotranspiration Models of the Nagqu River Basin of the Tibetan Plateau. *Journal of Geophysical Research: Atmospheres*, *123*(8), 3961–3975. https://doi.org/10.1002/2017JD027965

Zhang, Y., Kong, D., Gan, R., Chiew, F. H. S., McVicar, T. R., Zhang, Q., & Yang, Y. (2019). Coupled estimation of 500 m and 8-day resolution global evapotranspiration and gross primary production in 2002–2017. *Remote Sensing of Environment*, *222*, 165–182. https://doi.org/10.1016/j.rse.2018.12.031